Faraday effect in graphene enclosed in an optical cavity and the equation of motion method for the study of magneto-optical transport in solids

Aires Ferreira, J. Viana-Gomes, Yu. V. Bludov, V. Pereira, N. M. R. Peres, and A. H. Castro Neto

Phys. Rev. B **84**, 235410 — Published 1 December 2011

DOI: 10.1103/PhysRevB.84.235410

Faraday effect in graphene enclosed in an optical cavity and the equation of motion method for the study of magneto-optical transport in solids

Aires Ferreira[1,2], J. Viana-Gomes[1], Yu. V. Bludov[1], V. Pereira[2], N. M. R. Peres[1,2], A. H. Castro Neto[2,3]
[1] *Department of Physics and Center of Physics, University of Minho, P-4710-057, Braga, Portugal*
[2] *Graphene Research Centre and Department of Physics, National University of Singapore, 2 Science Drive 3, Singapore 117542 and*
[3] *Department of Physics, Boston University, 590 Commonwealth Avenue, Boston, Massachusetts 02215, USA*
(Dated: November 7, 2011)

We show that by enclosing graphene in an optical cavity, giant Faraday rotations in the infrared regime are generated and measurable Faraday rotation angles in the visible range become possible. Explicit expressions for the Hall steps of the Faraday rotation angle are given for relevant regimes. In the context of this problem we develop an equation of motion (EOM) method for the calculation of the magneto-optical properties of metals and semiconductors. It is shown that properly regularized EOM solutions are fully equivalent to the Kubo formula.

PACS numbers:

I. INTRODUCTION

Electromagnetic radiation emitted by far stellar objects travels for long periods of time through very diluted concentrations of interstellar gases, traversing regions where week magnetic fields exist. In this circumstance, the polarization of the electric field rotates due to its interaction with the gases immersed in the magnetic field. Due to the enormous traveling distances through such interstellar regions, the degree of rotation of the polarization can be important. This magnetic rotational effect turns out to be a problem in astrophysics, since it modifies, in an unpredictable way, the polarization state of the emitted radiation, introducing additional difficulties in the interpretation of the astronomical observations. In the electrodynamics of metals and insulators the effect of polarization rotation induced by a magnetic field was first discussed by Faraday[1], and on Earth has many different applications.

In magneto-optics, the effect coined optical Faraday rotation[1] refers to the rotation of the plane of polarization of light when it transverses either a dielectric[2] or a metal[3], in the presence of a static magnetic field applied along the direction of propagation of the electromagnetic wave. In addition to the rotation of the plane of polarization, the polarization itself acquires a certain degree of ellipticity. In dielectrics, the effect can be explained using a model of harmonic oscillators coupled to light.[2] In metals, the effect has its roots in the Hall effect.[4]

For a two-dimensional metal, such as graphene, in the Hall regime, the conductivity becomes a tensor, $\hat{\sigma}$, with finite (non-zero) values for both diagonal and off-diagonal components. In magneto-optics, the components of the tensor depend both of the frequency of the impinging electromagnetic wave and on the cyclotron frequency of the electrons, due to the magnetic field perpendicular to the plane of the metal. The response of the electrons to the external magnetic field has two different regimes: (i) the semi-classical limit, of low fields or/and high electronic density; (ii) the quantum Hall regime, of strong fields or/and low electronic density.

For the interpretation of the optical Faraday rotation, in the semi-classical regime, Drude theory of metals suffices.[3] In the case of graphene, it is possible to change its electronic density either by using a gate or by the adsorption of molecules.[5,6] At large doping, graphene is in the semiclassical regime and Boltzmann transport theory can be used to compute the Hall conductivity.[7]

In the absence of disorder and other relaxation mechanisms (such as electron-phonon scattering), the conductivity of graphene (at zero magnetic field) would be exclusively determined by interband transitions. In the limit of no disorder, the optical conductivity of doped graphene, in the infrared region of the spectrum and at zero magnetic field, is given by[8–15]

$$\sigma_{xx} = \sigma_{\rm g} n_F(\hbar\omega - 2E_F)\,, \tag{1}$$

where $\sigma_{\rm g} = \pi e^2/(2h)$ is the so-called ac universal conductivity of graphene.[8,16–18]

When a magnetic field is applied perpendicularly to graphene's surface, the system develops a finite Hall conductivity. In the quantum regime, it was shown that Faraday rotation angle θ_F is solely determined by the fine structure constant α, and presents a step-like structure as the Fermi energy crosses different Landau levels (LLs).[19] The estimated Faraday rotation steps' height in this case is of order of $\theta_F \sim 0.4^\circ$,[19] a magnitude that can be resolved experimentally.[20] In the context of topological insulators, similar quantization rules in particular thin-film geometries have been derived in Refs. 21 and 22. We note in passing that, when the external magnetic field is absent, a dynamic Hall effect can still be induced by using circularly polarized light impinging on graphene at a finite angle with the normal to the graphene surface.[23]

In the theoretical side, the magneto-optical transport properties of graphene have been investigated with the Green's function method[8,10], and by means of numerical implementations of the Kubo formula, us-

ing exact diagonalization[19] and Chebyshev polynomial expansions.[24] These approaches come with pros and cons: numerical studies allow to explore general scenarios, whereas Green's functions allows to obtain analytic results, but many times at the expense of a lengthy calculations.

Motivated by the need for analytical flexible analytical tools, the equation of motion (EOM) method employed in Ref. 25 is generalized as to include the effect of a magnetic field. As shown later, starting from a small set of EOMs, an adequate treatment permits the derivation of the response functions with correct analytical properties (i.e., satisfying Kramers-Kronig causality relations).

The present paper is divided in two main parts. In Sec. II we present the EOM method for the calculation of the magneto-optical transport in metals and semiconductors; to be concrete the method is described in the context of the properties of graphene. In Sec. III we describe in detail the Faraday effect in graphene and propose an experimental setup that is able to enhance the Faraday effect up to the visible range. Sec. III relies heavily in the results derived earlier in Sec. II. Several technical details are given in Appendix.

We have chosen to organize the subjects according to the following interests of the different readers: the reader having a primary interest on the Faraday effect, and familiar with all the details about the magneto-optical properties of graphene, should be able to read Sec. III with a bird's eye reading of Sec. II. The reader interested in the Faraday effect in graphene but not well acquainted with its magneto-optical properties may want to go through Sec. II first. Finally, the reading of Sec. II alone may appeal to those readers interested in applying the equation of motion method to another problem of interest bearing no relation to graphene.

II. EQUATION OF MOTION METHOD FOR THE CALCULATION OF THE MAGNETO-OPTICAL CONDUCTIVITY

In the forthcoming sub-section, we develop the equation of motion approach to the calculation of the magneto-optical properties of a semiconductor. To be concrete, the method is presented in the context of the optical response of graphene. The magneto-optical response of graphene was used before in the study of Faraday rotation in graphene.

Electrons constrained to two dimensions are responsible for a variety of quantum manifestations, a striking example being the integer quantum Hall effect (IQHE). Measured in semiconductor 2D electron gases more than 30 years ago[26] and in the yearly days of graphene, in both monolayer[5,27] and bilayer samples[28] (very recently also in trilayer graphene[29]), the static quantum Hall effect is an hallmark elementary of excitations in electronic systems.[30]

Its dynamical analogue—the ac quantum Hall effect—can provide additional information about charge carriers, such as the opening of gaps in the spectrum.[31] Recent advances in time-domain spectroscopy in the Thz regime[20] have paved the way to measure the dynamical optical conductivities at impinging field energies closer to the scale of interest. The goal is to reach cyclotronic energies, usually $\mathcal{O}(10)$meV in fields 1-10 T, whereof strong optical responses take place. The so-called *optical* quantum Hall conductivity of 2D electron gases shows robust plateaux as the Fermi energy is swept, although no quantization rule for the plateaux's height exists.[32] Due to its peculiar band structure, graphene has been predicted to display a characteristic optical quantum Hall effect which should be detectable via Faraday rotation measurements.[19] In the semi-classical regime, on the other hand, the Faraday rotation of graphene was reported to be $\mathcal{O}(1)$ degrees in fields of a few tesla[33], a surprisingly high value for an one-atom thick electronic system.

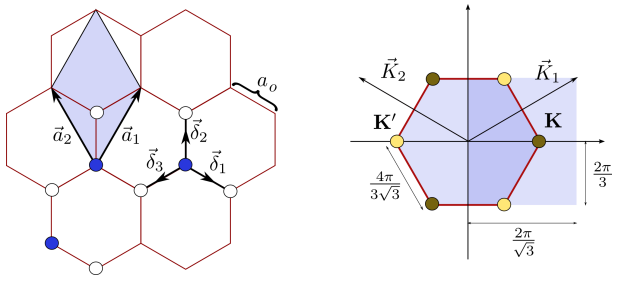

Figure 1: (Color online) Lattice structure and Brillouin zone of monolayer graphene. **Left:** Hexagonal lattice of graphene, with the next nearest neighbor, $\boldsymbol{\delta}_i$, and the primitive, $\boldsymbol{a}_i$, vectors depicted. The area of the primitive cell is $A_c = 3\sqrt{3}a_0^2/2 \simeq 5.1$ Å^2, and $a_0 \simeq 1.4$ Å. **Right:** Brillouin zone of graphene, with the Dirac points $\boldsymbol{K}$ and $\boldsymbol{K}'$ indicated. Close to these points, the dispersion of graphene is conical and the density of states is proportional to the absolute value of the energy.

A. Graphene

The starting point of the present analysis is the low-energy continuum description of single-layer graphene; having two (carbon) atoms per unit cell and six-fold symmetry, its elementary excitations obey a 2D Dirac equation with linear electronic dispersion.[34] This subsection is meant to fix the notation. The Brillouin zone of graphene has six corners and among these only two are inequivalent, the so-called **K** and **K**′ Dirac points (see Fig. 1). At these points, the valence and conduction bands touch, with linear electronic spectrum up to energies ∼2eV.

We assume, in what follows, that the two Dirac points can be treated independently, and introduce the valley degeneracy index, $g_v = 2$, when pertinent. This consideration is justified for typical experimental conditions (i.e., low concentrations of scattering centers, finite

temperatures, etc.) and provides an accurate description of graphene's electronic transport properties at finite densities.[16,35]

In accordance, we resort to the 2×2 Dirac Hamiltonian of graphene, describing the physics of elementary excitations within the $\mathbf{K}$ valley, $H_{\mathbf{K}} = v_F \boldsymbol{\sigma} \cdot \mathbf{p}$, where $v_F \simeq 10^6$m/s is the Fermi velocity, $\boldsymbol{\sigma} = (\sigma_x, \sigma_y)$ [with σ_i $(i = x, y)$ denoting Pauli matrices], and $\mathbf{p}$ is the momentum of the low-energy excitation (measured relative to the $\mathbf{K}$ point).[34] $H_{\mathbf{K}}$ has eigenvalues given by

$$E = \pm \hbar v_F |\mathbf{k}| \,, \tag{2}$$

[with $\mathbf{k} = (k_x, k_y)$ denoting a two-dimensional wave vector], and (normalized) wavefunctions given by

$$\psi_{\lambda,\mathbf{k}}(\mathbf{r}) = \frac{1}{\sqrt{2A}} \begin{pmatrix} 1 \\ \lambda e^{i\theta_{\mathbf{k}}} \end{pmatrix} e^{i\mathbf{k}\cdot\mathbf{r}} \,, \tag{3}$$

where A is the area of the graphene sample, $\lambda = +1(-1)$ for electron(hole)-like excitation, and $\theta_{\mathbf{k}} = \arctan(k_y/k_x)$.

The electromagnetic field can be incorporated via minimal coupling, $\mathbf{p} \to \mathbf{p} + e\mathbf{A}_{\rm g}$, where $-e < 0$ is the electron charge, and the vector potential $\mathbf{A}_{\rm g}$ relates to the electromagnetic field according to the usual relations, $\mathbf{B} = \boldsymbol{\nabla} \times \mathbf{A}_{\rm g}$ and $\mathbf{E} = -\partial \mathbf{A}_{\rm g}/\partial t$.

Here, the vector potential contains the information about the impinging electromagnetic radiation, and possible external static magnetic fields. Assuming light linearly polarized along the x-axis, the radiation term reads $\mathbf{A} = [A_0(\mathbf{r})e^{-i\omega t} + \text{c.c.}]\mathbf{e}_{\mathbf{x}}$, where ω stands for the frequency of the radiation field and $A_0(\mathbf{r})$ describes its position dependence. For clarity of exposition, we separate the light-matter interaction term from the free Hamiltonian,

$$H = H_0 + e v_F \boldsymbol{\sigma} \cdot \mathbf{A} \,, \tag{4}$$

where $H_0 \equiv H_{\mathbf{K}} + e v_F \boldsymbol{\sigma} \cdot \mathbf{A}_B$, with $\mathbf{A}_B$ describing the static magnetic field.

A typical experimental scenario corresponds to a constant magnetic field $B > 0$ applied in the transverse direction with respect to the graphene plane. In such case, LLs develop and the eigenenergies of charge carriers become quantized according to[36]

$$E_n = \text{sign}(n) \frac{\hbar v_F}{l_B} \sqrt{2|n|} \quad , n = 0, \pm 1, \pm 2, ..., \tag{5}$$

with $l_B = \sqrt{\hbar/(eB)}$ denoting the magnetic length. Choosing the gauge $\mathbf{A}_B = (0, Bx, 0)$ results in the following set of Landau eigenfunctions,

$$\psi_{n,k_y}(\mathbf{r}) = \frac{C_n}{\sqrt{L}} \begin{pmatrix} \phi_{|n|-1}(x) \\ i\text{sign}(n)\phi_{|n|}(x) \end{pmatrix} e^{ik_y y} \,, \tag{6}$$

where $\phi_n(x) = e^{-\xi(x)^2/2} H_n(\xi(x))/\sqrt{n! 2^n \sqrt{\pi} l_B}$, $H_n(x)$ is the Hermite polynomial of degree $n \geq 0$, $\phi_{-1}(x) = 0$, and $\xi(x)$ stands for the dimensionless center of the Landau orbit, $\xi(x) = l_B k_y + x/l_B$. Here, L is the linear dimension of the system in the y direction and C_n is a normalization constant that distinguishes the zero-energy level from the remaining levels, $C_n = 1$ for $n = 0$ and $C_n = 1/\sqrt{2}$ for $|n| \geq 1$.

Having reviewed the basics of the graphene's electronic low energy theory, in what follows we present the EOM approach to the study of magneto-optical transport.

B. Theoretical methods

In the context of electronic systems, the EOM was extensively used in calculations of light polarization in semiconductor laser theory.[37] Recently, it has been used to study excitons in graphene in zero field.[25]

The EOM approach avoids the calculation of current-current correlators (i.e. Kubo formula), and hence provides a shortcut to the determination of response of electronic systems to external perturbations. As shown in detail in Appendix C, with an appropriate regularization procedure, the EOM solutions become fully equivalent to the Kubo formula, and hence provide an accurate description of transport in the linear response regime. Another advantage of the present approach is that it allows for the calculation of non-linear corrections to the conductivity.[38]

At the heart of the EOM approach to the calculation of the magneto-optical conductivity is the Heisenberg equation for the electronic current density, $\boldsymbol{J}(t)$, in the presence of an external electromagnetic field, i.e., $d\boldsymbol{J}/dt = (i/\hbar)[H, \boldsymbol{J}]$, with H being the total Hamiltonian, Eq. (4). Having solved for the current density of the system in the presence of the external perturbation, in first order in the external field $\mathbf{A}$, the optical conductivity follows from the constitutive electromagnetic relation

$$\sigma_{ij}(\omega) = g_s g_v \times \frac{\tilde{J}_i(\omega)}{\tilde{E}_j(\omega)} \,, \tag{7}$$

where $\tilde{O}(\omega)$ relates to the average $O(t)$ $[O = J_i, E_j]$ according to $O(t) = \tilde{O}(\omega)e^{-i\omega t} + \text{c.c.}$, with appropriate regularization implicit (Appendix C; Sec. II D). Having graphene in the Dirac cone approximation in mind, the latter equation contains the relevant degeneracies. The spin contribution as a degeneracy factor, g_s, should be valid for typical magnetic fields ($\lesssim$15 T) when the Zeeman effect does not manifest.

The first step is to project the Heisenberg equation of motion for the current onto the space of unperturbed single-particle states: we introduce the field operator $\Psi_\sigma(\mathbf{r}, t) = \sum_{\boldsymbol{\alpha}} \hat{c}_{\boldsymbol{\alpha},\sigma}(t)\psi_{\boldsymbol{\alpha}}(\mathbf{r})$ (and respective hermitian conjugate), where $\hat{c}_{\boldsymbol{\alpha},\sigma}(\hat{c}^\dagger_{\boldsymbol{\alpha},\sigma})$ is the annihilation (creation) operator obeying fermionic anti-commutation rules: $\{\hat{c}_{\boldsymbol{\alpha},\sigma}, \hat{c}^\dagger_{\boldsymbol{\alpha}',\sigma'}\} = \delta_{\boldsymbol{\alpha}\boldsymbol{\alpha}'}\delta_{\sigma,\sigma'}$ and $\{\hat{c}_{\boldsymbol{\alpha},\sigma}, \hat{c}_{\boldsymbol{\alpha}',\sigma'}\} = \{\hat{c}^\dagger_{\boldsymbol{\alpha},\sigma}, \hat{c}^\dagger_{\boldsymbol{\alpha}',\sigma'}\} = 0$. The symbol $\boldsymbol{\alpha} = (\lambda, \mathbf{k}, ...)$ specifies the single-particle state of the electron (or hole) and $\sigma = \pm 1$

is the spin variable. The kets $|\boldsymbol{\alpha},\sigma\rangle \equiv \hat{c}^{\dagger}_{\boldsymbol{\alpha},\sigma}|0\rangle$ represent eigenstates of H_0, and, therefore, the position representation, $\langle \mathbf{r}|\boldsymbol{\alpha},\sigma\rangle \equiv \psi_{\boldsymbol{\alpha},\sigma}(\mathbf{r})$, equals Eq. (3) at zero magnetic field or Eq. (6) in the presence of a transverse uniform magnetic field.

The second-quantized form of the full Hamiltonian and the current density operator is given by

$$\hat{H}(t) = \sum_{\sigma} \int d\mathbf{r} \Psi^{\dagger}_{\sigma}(\mathbf{r},t) H \Psi_{\sigma}(\mathbf{r},t)\,, \tag{8}$$

$$\hat{J}_i(t) = \sum_{\sigma} \int d\mathbf{r} \Psi^{\dagger}_{\sigma}(\mathbf{r},t) j_i \Psi_{\sigma}(\mathbf{r},t)\,, \tag{9}$$

respectively, where,

$$\boldsymbol{j} = -\frac{ev_F}{A}\boldsymbol{\sigma}\,, \tag{10}$$

is the current density of graphene in the continuum description.[16,35] We omit the spin dependence of the operators hereafter for clarity of exposition.

We now define the generic operator,

$$\hat{P}_{\boldsymbol{\alpha\beta}}(t) \equiv \hat{c}^{\dagger}_{\boldsymbol{\alpha}}(t)\hat{c}_{\boldsymbol{\beta}}(t)\,, \tag{11}$$

whose EOM reads

$$\frac{d}{dt}\hat{P}_{\boldsymbol{\alpha\beta}}(t) = \frac{i}{\hbar}\sum_{\boldsymbol{\gamma},\boldsymbol{\delta}} h_{\boldsymbol{\gamma\delta}} \left[\hat{P}_{\boldsymbol{\gamma\delta}}(t),\, \hat{P}_{\boldsymbol{\alpha\beta}}(t)\right]\,, \tag{12}$$

where $h_{\boldsymbol{\gamma\delta}} = \langle \boldsymbol{\gamma}|\hat{H}|\boldsymbol{\delta}\rangle$ are the matrix elements of the full Hamiltonian [Eq. (4)]. Solving for $\hat{P}_{\boldsymbol{\alpha\beta}}(t)$ gives directly the current density according to,

$$\hat{J}_i(t) = \sum_{\boldsymbol{\alpha},\boldsymbol{\beta}} \langle \boldsymbol{\alpha}|j_i|\boldsymbol{\beta}\rangle \hat{P}_{\boldsymbol{\alpha\beta}}(t), \tag{13}$$

and hence the (yet non-regular) optical conductivity via Eq. (7). The regularization is the final step of the EOM approach needed for obtaining a fully-consistent conductivity (in particular, obeying Kramers-Kronig relations).[39] The respective technical procedure is given in Appendix C.

In the following section, we solve explicitly Eq. (12) in the linear response regime (i.e. first order in the electric field) for any pair of quantum states $\boldsymbol{\alpha}$,$\boldsymbol{\beta}$, in the absence of a magnetic field. The case of finite (non-zero) magnetic field intensity is left to Sec. II D.

C. Graphene in zero magnetic field

The purpose of this section is to show the equation of motion method at work in the context of a simple problem, which allow us to derive well known results.

In the absence of magnetic fields, the macroscopic electronic current follows the applied optical field, and thus only the longitudinal conductivity is non-zero. From symmetry considerations, we also have $\sigma_{xx}(\omega) = \sigma_{yy}(\omega)$.

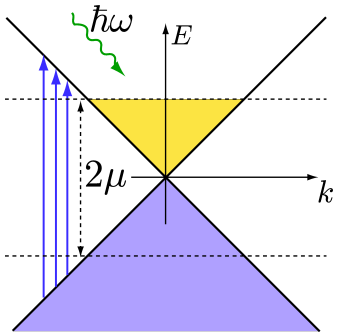

Figure 2: Allowed interband transitions (vertical arrows) in graphene; a photon of energy $\hbar\omega$ produces an excitation from the lower to the upper Dirac, as long as $\hbar\omega > 2\mu$. The transitions conserve $\mathbf{k}$ and hence are said to be "vertical". For $\hbar\omega \leq 2\mu$, Pauli blocking forbids any (interband) transition. In practice, due to disorder (impurities, etc.), the interband conductivity can be non-zero even for $\hbar\omega \leq 2\mu$.

According to the statement Eq. (13), the relevant set of EOM to be solved is determined by the non-zero matrix elements of the current density.

Defining $\langle \mathbf{k},\lambda|j_x|\mathbf{k}',\lambda'\rangle = -(ev_F/A)j^x_{\lambda,\lambda',\mathbf{k},\mathbf{k}'}$ and using the wavefunctions Eq. (3), we easily find

$$j^x_{\lambda,\lambda',\mathbf{k},\mathbf{k}'} = \frac{\delta_{\mathbf{k},\mathbf{k}'}}{2}\left(\lambda' e^{i\theta_{\mathbf{k}}} + \lambda e^{-i\theta_{\mathbf{k}}}\right)\,. \tag{14}$$

With this notation, the current density along the x direction reads,

$$J_x(t) = -\frac{ev_F}{A}\sum_{\lambda,\lambda',\mathbf{k}} j^x_{\lambda,\lambda',\mathbf{k},\mathbf{k}} \langle \hat{c}^{\dagger}_{\lambda,\mathbf{k}}(t)\hat{c}_{\lambda',\mathbf{k}}(t)\rangle\,. \tag{15}$$

The non-null matrix elements in Eq. (14) contributing to the conductivity correspond to transitions between different bands conserving the momentum $\mathbf{k}$. These transitions are said to be "vertical" and, in addition, since they connect states in different bands, they are refereed to as being interband-like (see Fig. 2).

Taking the dipole approximation, $A(\mathbf{r}) \to A_0$, the Hamiltonian [Eq. (8)] reads

$$\hat{H} = \sum_{\lambda,\mathbf{k}} E_{\lambda}(\mathbf{k})\hat{c}^{\dagger}_{\lambda,\mathbf{k}}\hat{c}_{\lambda,\mathbf{k}} + ev_F A_0\left(e^{-i\omega t} + \text{c.c.}\right)\times \\ \times \sum_{\mathbf{k}} j^x_{c,v,\mathbf{k},\mathbf{k}}\hat{c}^{\dagger}_{c,\mathbf{k},\sigma}\hat{c}_{v,\mathbf{k},\sigma} + (c \longleftrightarrow v)\,. \tag{16}$$

In the latter equation, $E_{\lambda}(\mathbf{k}) \equiv \lambda\hbar v_F k$, and the subscripts c (v) denote electrons (holes).

As described in above, we need to compute the time evolution of the operator $\hat{P}_{v,c,\mathbf{k}}(t) = \hat{c}^{\dagger}_{v,\mathbf{k}}(t)\hat{c}_{c,\mathbf{k}}(t)$. Straightforward algebra yields,

$$\frac{d}{dt}\hat{P}_{v,c,\mathbf{k}} = \frac{i}{\hbar}\Big\{\left[E_v(\mathbf{k}) - E_c(\mathbf{k})\right]\hat{P}_{v,c,\mathbf{k}} \\ + ev_F A_0\left(e^{-i\omega t} + \text{c.c.}\right) j^x_{c,v,\mathbf{k},\mathbf{k}}\left[\hat{n}_c(t) - \hat{n}_v(t)\right]\Big\}\,, \tag{17}$$

where we have defined the occupation operator for electrons (holes) as $\hat{n}_{c(v)}(t) \equiv \hat{c}^{\dagger}_{c(v),\mathbf{k}}(t)\hat{c}_{c(v),\mathbf{k}}(t)$. A similar equation holds for $\hat{P}_{c,v,\mathbf{k},\sigma}$ which can be obtained by interchanging $c \longleftrightarrow v$.

To proceed, we take the average of Eq. (17) with respect to the unperturbed Hamiltonian, H_0, and approximate $\langle \hat{n}_c(t) - \hat{n}_v(t)\rangle_0 \simeq \langle \hat{n}_c - \hat{n}_v\rangle_0$. Both procedures are consistent with an expansion of $\hat{J}_x(t)$ up to first order in the parameter A_0. The solution of the above differential equation reads

$$\langle \hat{P}_{v,c,\mathbf{k}}(t)\rangle_0 = \tilde{P}_{v,c,\mathbf{k}}(\omega)e^{-i\omega t} + \tilde{P}_{v,c,\mathbf{k}}(-\omega)e^{i\omega t}\,, \quad (18)$$

with,

$$\tilde{P}_{v,c,\mathbf{k}}(\omega) \;=\; ev_F A_0 j^x_{c,v,\mathbf{k},\mathbf{k}} \frac{\langle \hat{n}_c\rangle_0 - \langle \hat{n}_v\rangle_0}{E_c(\mathbf{k}) - E_v(\mathbf{k}) - \hbar\omega - i\Gamma}, \quad (19)$$

and we have introduced a imaginary energy Γ by hand, as to account for disorder phenomenologically. The remaining term $\tilde{P}_{v,c,\mathbf{k},\sigma}(\omega)$ can be obtained from the latter expression by making $\omega \to -\omega$ and $\Gamma \to -\Gamma$. From Eq. (15), the oscillator strength of the current density along the x direction $\tilde{J}_x(\omega)$ is seen to be given by

$$\tilde{J}_x(\omega) = -\frac{ev_F}{A}\sum_{\mathbf{k}}[j^x_{v,c,\mathbf{k},\mathbf{k}}\tilde{P}_{v,c,\mathbf{k}}(\omega) + j^x_{c,v,\mathbf{k},\mathbf{k}}\tilde{P}_{c,v,\mathbf{k}}(\omega)]\,. \quad (20)$$

The longitudinal optical conductivity, σ_{xx}, follows from Eq. (7),

$$\sigma^{\rm inter}_{xx}(\omega) = g_v g_s \frac{e^2 v_F^2}{i\omega}\int \frac{d^2\mathbf{k}}{4\pi^2}\left(\sin^2\theta_{\mathbf{k}}\right)\times \times \frac{n_F\left[E_v(\mathbf{k})\right] - n_F\left[E_c(\mathbf{k})\right]}{E_c(\mathbf{k}) - E_v(\mathbf{k}) - \hbar\omega - i\Gamma} + (c \leftrightarrow v)\,. \quad (21)$$

where $n_F(E) = 1/[e^{(E-\mu)/k_BT} + 1]$ stands for the Fermi-Dirac distribution (μ is the chemical potential). In deriving this expression, we have used the relation $\tilde{E}_x(\omega) = i\omega A_0$. Taking the clean limit $\Gamma \to 0$ and considering $\omega > 0$ and $T = 0$, one obtains the well known-result

$$\mathrm{Re}\;\sigma^{\rm inter}_{xx}(\omega) \;=\; \frac{\pi e^2}{2h}\theta\left(\hbar\omega - 2|\mu|\right)\,. \quad (22)$$

The latter result is the $T \to 0$ limit of Eq. (1). For photon energies greater than 2μ (see Fig. 2), the interband conductivity is essentially frequency independent (up to energies $\sim$2 eV) and equals

$$\sigma_{\rm g} = \frac{\pi e^2}{2h}\,, \quad (23)$$

which is nothing else than the universal conductivity of graphene mentioned in the Introduction. For $\mu = 0$, and contrary to ordinary semiconductors, there is no frequency threshold for interband transitions: according to Eq. (22) some interband transitions will always be available for sufficiently high photon frequency. As a consequence, Drude's description will not suffice for a general description of the optical response of graphene.

On top of the interband transitions discussed here, there is an intraband contribution in graphene which can be appreciable for $\mu \neq 0$. This contribution comes from non-vertical processes (e.g. via collisions with phonons), not included in the Hamiltonian Eq. (16). This contribution gives the Drude response and reads[40]

$$\mathrm{Re}\,\sigma^{\rm intra}_{xx}(\omega) = \frac{2e^2}{h}|\mu|\frac{\Gamma}{\hbar^2\omega^2 + \Gamma^2}\,. \quad (24)$$

Interestingly enough, the latter result can be derived from a full quantum mechanical calculation by considering a finite magnetic field intensity and taking the limit $B \to 0$ in the end.[10] This is because a magnetic field open gaps in the spectrum of the clean system, allowing for intraband transitions (see Sec. II D). A semi-classical calculation also leads to an equivalent result (Sec. II E).

D. Optical conductivity of graphene in a magnetic field

In what follows, we show that the EOM method can be employed to study the magneto-optical response of graphene along the same lines of Sec. II C. The presence of a transverse magnetic field in the Hamiltonian develops LLs, and hence we must start from the eigenstates given in Eq. (6). The latter defines the field operator, $\Psi(\mathbf{r},t) = \sum_{n,k_y}\hat{c}_{n,k_y}(t)\psi_{n,k_y}(\mathbf{r})$ (together with the respective hermitian conjugate); the index n labels the degenerate LL with energy given by Eq. (5). The field operator can be written as

$$\Psi(\mathbf{r},t) \;=\; \frac{1}{\sqrt{2L}}\sum_{n\neq 0,k_y}\begin{pmatrix}\phi_{|n|-1}(x)\\ i\mathrm{sign}(n)\phi_{|n|}(x)\end{pmatrix}e^{ik_y y}\hat{c}_{n,k_y} + \frac{1}{\sqrt{L}}\sum_{k_y}\begin{pmatrix}0\\ \phi_0(x)\end{pmatrix}e^{ik_y y}\hat{c}_{0,k_y}\,. \quad (25)$$

This peculiar spinorial structure, with a single level being highlighted, is on the basis of non-standard features in the magneto-optical conductivity of graphene.[8,11,31,41]

1. *The longitudinal conductivity*

According to Eq. (7), the calculation of the longitudinal conductivity requires the computation of the average value of the current density operator along the x direction,

$$J_x(t) = \sum_{n,n'}\sum_{k_y,k'_y}\langle n,k_y|j_x|n',k'_y\rangle\langle \hat{c}^{\dagger}_{n,k_y}(t)\hat{c}_{n',k'_y}(t)\rangle\,. \quad (26)$$

Using the LL wavefunctions [Eq. (6)], we easily find the non-zero matrix elements to be,

$$\langle 0,k_y|j_x|\pm 1,k_y'\rangle = -\frac{ev_F}{\sqrt{2}A}\delta_{k_y,k_y'}\,, \tag{27}$$

$$\langle n,k_y|j_x|n',k_y'\rangle = -\frac{ev_F}{2A}i\left[\mathrm{sign}(n')\delta_{|n|-1,|n'|} - \mathrm{sign}(n)\delta_{|n|,|n'|-1}\right]\delta_{k_y,k_y'}\,, \tag{28}$$

where in the last line $n, n' \neq 0$. These statements show that the optical transitions conserve k_y and occur between levels with indexes n and n' differing by the unit, i.e., $|n| - |n'| = \pm 1$.

Two sets of transitions are thus allowed: intraband transitions, occurring within the same band, and, as in the absence of magnetic field, transitions connecting LLs in the valence and conduction bands, which are interband-like. Transitions involving the zero energy state $n = 0$ can either be considered intraband or interband-like, since the zero-energy state is shared between electrons and holes. For sake of simplicity in defining the set of EOMs, throughout, we classify the transitions involving the zero energy state as being interband.

In order to clearly distinguish between the possible types of transitions, we define

$$\hat{c}_{n,k_y} \equiv \begin{cases} c_n & \text{for } n > 0 \\ v_{|n|} & \text{for } n < 0 \\ a_0 & \text{for } n = 0 \end{cases}\,, \tag{29}$$

with the hermitian conjugates following identical redefinitions. Note that with these definitions the subscript n in the operators take only positive integer values.

Interband transitions.—Using the field operator in the presence of a magnetic field [Eq. (25)], and just keeping track of the interband terms for the moment being, the full Hamiltonian takes the following form,

$$\hat{H} = \sum_{n\geq 1}\left[E_n c_n^\dagger c_n + E_{-n} v_n^\dagger v_n\right] + \frac{ev_F A(t)}{\sqrt{2}}\left[c_1^\dagger a_0 + v_1^\dagger a_0 + \text{h.c.}\right] - \frac{ev_F A(t)}{2}i\sum_{n\geq 1}\left[\hat{P}_n^{(1)} + \hat{P}_n^{(2)} - \text{h.c.}\right]\,, \tag{30}$$

where $A(t) \equiv A_0(e^{-i\omega t} + \text{c.c.})$, and

$$\hat{P}_n^{(1)} = c_n^\dagger v_{n+1}\,, \tag{31}$$

$$\hat{P}_n^{(2)} = c_{n+1}^\dagger v_n\,. \tag{32}$$

(Also, for clarity, we have omitted k_y under all the summation signs.) The first line in Eq. (30) describes massless Dirac fermions in a transverse magnetic field and the remaining lines contain the electronic transitions among different LLs induced by the external electric field.

The interband current density along the x direction can be recast into the form

$$\hat{J}_x(t) = -\frac{1}{\sqrt{2}A}ev_F\left(c_1^\dagger a_0 + v_1^\dagger a_0 + \text{h.c.}\right) + \frac{1}{2A}ev_F\sum_{n\geq 1}\left(i\hat{P}_n^{(1)} + i\hat{P}_n^{(2)} + \text{h.c.}\right)\,. \tag{33}$$

From the form of the current we see that there are two basic sets of EOMs to be solved: a first set refers to the time evolution of operators involving the zero-energy state ($c_1^\dagger a_0$, $v_1^\dagger a_0$ and hermitian conjugates), while the other set refers to higher energy LLs. Take for instance the operator $\hat{P}_n^{(1)}$ belonging to the latter set; as in the case of zero magnetic field (Sec. II C), the commutator $[H, \hat{P}_n^{(1)}]$ gives rise to i) occupation number operators ($v_{n+1}^\dagger v_{n+1}$ and $c_n^\dagger c_n$), and ii) a free evolution term, that is, the operator $\hat{P}_n^{(1)}$ itself. In addition, intraband terms with $|n| - |n'| = \pm 2$ show up, namely, $c_n^\dagger c_{n+2}$, $v_{n-1}^\dagger v_{n+1}$ and $a_0^\dagger v_2 \delta_{n,1}$. These terms do not originate real intraband transitions, since the respective current density matrix elements are null.

We are now in position to write the prototype EOMs governing the interaction of Landau quasi-particles with an external oscillating electric field,

$$\frac{\hbar}{i}\frac{d}{dt}\hat{P}_n^{(1)} = \left[E_n - E_{-(n+1)}\right]\hat{P}_n^{(1)} - \frac{i}{2}ev_F A(t)\times \times\left[v_{n+1}^\dagger v_{n+1} - c_n^\dagger c_n\right]\,, \tag{34}$$

$$\frac{\hbar}{i}\frac{d}{dt}\hat{P}_c = E_1\hat{P}_c + \frac{1}{\sqrt{2}}ev_F A(t)[a_0^\dagger a_0 - c_1^\dagger c_1]\,, \tag{35}$$

where we have omitted the time dependence of the operators and defined $\hat{P}_{c(v)} = c(v)_1^\dagger a_0$. The remaining operators obey similar equations. [The EOM for $\hat{P}_n^{(2)}$ is obtained making $\hat{P}_n^{(1)} \to \hat{P}_n^{(2)}$and interchanging n with $n+1$ in the right-hand side of Eq. (34). As for $\hat{P}_v$, we let $\hat{P}_c \to \hat{P}_v$, $E_1 \to E_{-1}$ and $c_1(c_1^\dagger) \to v_1(v_1^\dagger)$ in Eq. (35).]

To solve the above set of differential equations in first order in A_0, we proceed as in Sec. II C. Taking the average value $\langle ...\rangle_0$ of each EOM with respect to the unperturbed Hamiltonian, H_0, the solution for each operator O can be written as $\langle O(t)\rangle_0 = \tilde{O}(\omega)e^{-i\omega t} + \tilde{O}(-\omega)e^{i\omega t}$, where the oscillator strengths read

$$\tilde{P}_n^{(1)}(\omega) = -\frac{i}{2}ev_F A_0\frac{\langle v_{n+1}^\dagger v_{n+1}\rangle_0 - \langle c_n^\dagger c_n\rangle_0}{E_{-(n+1)} - E_n - \hbar\omega - i\Gamma}\,, \tag{36}$$

$$\tilde{P}_c(\omega) = \frac{1}{\sqrt{2}}ev_F A_0\frac{\langle a_0^\dagger a_0\rangle_0 - \langle c_1^\dagger c_1\rangle_0}{-E_1 - \hbar\omega - i\Gamma}\,, \tag{37}$$

and where, as in Sec. II C, we have added a imaginary energy Γ to account for level broadening. The solutions for $\tilde{P}_n^{(2)}(\omega)$ and $\tilde{P}_v(\omega)$ can be obtained from the latter expressions as described below Eq. (35).

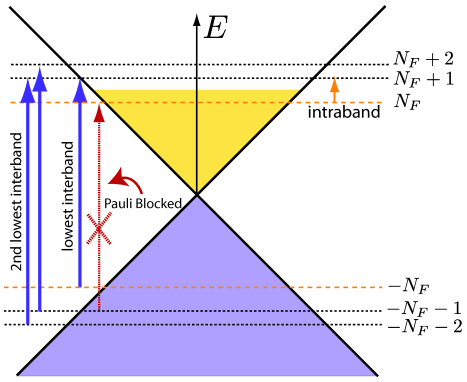

Figure 3: Schematic of electronic transitions contributing to $\sigma_{xx}(\omega)$ of doped graphene in a magnetic field. In this example, $E_F \geq E_1$, and thus the last occupied LL, $n = N_F \geq 1$, belongs to the conduction band. Two types of transitions take place: i) interband transitions, connecting LLs from the lower cone (valence band) with LLs in the upper cone (conduction band), and ii) intraband transitions within the upper cone. Intraband transitions are limited to adjacent LLs: $N_F \to N_F+1$. The picture shows the following interband transitions: a) the pair $-N_F \to N_F+1$ and $-N_F-1 \to N_F$, whose energy difference is $E_{N+1}+E_N$ (the lowest interband energy). Note that transitions $-N_F-1 \to N_F$ are forbidden because $n = N_F$ is occupied; b) the pair $-N_F-1 \to N_F+2$ and $-N_F-2 \to N_F+1$. The respective energy difference is $E_{N+1}+E_{N+2}$ (the second lowest interband energy difference) and in this case both transitions take place. Transitions with higher energy differences are not represented.

Combining these results and Eq. (33), we easily find

$$\tilde{J}_x(\omega) = \frac{1}{2A} e v_F \sum_{k_y} \left\{ \sum_{n\geq 1} \left[i\tilde{P}_n^1(\omega) + i\tilde{P}_n^2(\omega) \right] - \sqrt{2}\left[\tilde{P}_c(\omega) + \tilde{P}_v(\omega) \right] + \text{"c.c. term"} \right\} \quad (38)$$

where the summation over k_y has been restored. This summation yields the degeneracy of the Landau levels $\sum_{k_y} = A/(2\pi l_B^2)$. The last term in the above equation (i.e., the c.c. term) is obtained taking the complex conjugate and making $\omega \to -\omega$ of all the previous terms.

The final expression for the longitudinal (interband) conductivity is derived in two steps: 1) dividing the Eq. (38) by $\tilde{E}_x(\omega)$ [Eq. (7)], and 2) undertake appropriate regularization to remove the divergent factor $1/\omega$,

$$\sigma_{xx}^{\text{inter}}(\omega) = \frac{e^2 v_F^2 \hbar}{2\pi l_B^2} i \sum_{n=0}^{N_c} (1+\delta_{n,0}) \sum_{\alpha=\pm 1} \alpha \times \left[\frac{1}{E_{-(n+1)} - E_n} \times \frac{n_F[E_{-(n+1)}] - n_F[E_n]}{E_{-(n+1)} - E_n - \alpha(\hbar\omega + i\Gamma)} + (n \leftrightarrow n+1) \right] . \quad (39)$$

The above expression is analytic in the upper-half plane and finite at $\omega = 0$, thus obeying Kramers-Kronig causality relations. (We refer to Appendix C for the derivation and physical grounds of the regularization procedure.) Note that, as usual when dealing with low-energy theories, a cutoff energy E_{cut} of the order of bandwidth must be considered for consistency; we take $n \leq N_c$, with $N_c = \text{int}[(E_{\text{cut}}/E_1)^2]$, where int[...] denotes the integer part. N_c varies roughly as $10^4 B^{-1}$ with B in tesla. Within the physical relevant range for E_{cut}, these summations converge quite rapidly; the figures in the present work have $E_{\text{cut}} \approx t \simeq 2.7$ eV.

Intraband transitions.—The intraband interaction Hamiltonian reads

$$\hat{H}_{\text{int}}^{\text{intra}} = \frac{i}{2} e v_F A(t) \sum_{n\geq 1} \left[v_n^\dagger v_{n+1} - c_n^\dagger c_{n+1} - \text{h.c.} \right] , \quad (40)$$

and the zero energy operators (a_0 and $a_0^\dagger$) are absent given our classification of intraband transitions [see Eq. (29) and text therein]. The calculation follows identical steps to the interband conductivity, and hence will not be repeated. The final expression for the (regular) intraband diagonal conductivity reads,

$$\sigma_{xx}^{\text{intra}}(\omega) = \frac{e^2 v_F^2 \hbar}{2\pi l_B^2} i \sum_{\alpha=\pm 1} \alpha \sum_{n=1}^{N_c} \left[\frac{1}{E_{n+1} - E_n} \times \frac{n_F[E_{n+1}] - n_F[E_n]}{E_{n+1} - E_n - \alpha(\hbar\omega + i\Gamma)} + (E_n \to -E_n \wedge E_{n+1} \to -E_{n+1}) \right] . \quad (41)$$

The full longitudinal conductivity $\sigma_{xx}(\omega)$ is given by adding its interband and intraband counterparts, that is, Eqs. (39) and (41), respectively; straightforward algebra yields

$$\sigma_{xx}(\omega) = \frac{e^2}{h} \sum_{n\neq m=-N_c}^{N_c} \frac{\Lambda_{nm}^{xx}}{iE_{nm}} \frac{n_F(E_n) - n_F(E_m)}{\hbar\omega + E_{nm} + i\Gamma} , \quad (42)$$

with $E_{nm} = E_n - E_m$, and where we have defined the longitudinal matrix elements

$$\Lambda_{nm}^{xx} = \frac{\hbar^2 v_F^2}{l_B^2} (1 + \delta_{m,0} + \delta_{n,0}) \delta_{|m|-|n|,\pm 1} . \quad (43)$$

Equation (42) is the main result of the present section. It coincides with Eq. (7) of Ref. 42 obtained via a Green's function calculation in the bubble approximation, and also with a Kubo formula calculation within the Dirac cone approximation (see Appendix C). We note in passing that, on top of the interband and intraband contributions discussed here, there is a correction arising from phonon-electron coupling. At low temperatures and zero field, such correction is expected to be small.[40] At high magnetic field, though, a recent calculation shows that phonon energy peaks splits the LLs nearby,[43] which can lead to a measurable signature in magneto-optical experiments.

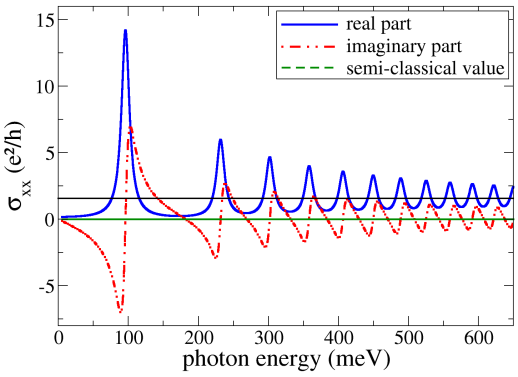

Figure 4: The longitudinal magneto-optical conductivity as function of the photon energy for a field of 7 T, zero chemical potential, $T = 17$ K and $\Gamma = 6.8$ meV (~ 79 K). The horizontal dashed-dot (black) line marks the graphene's universal ac-conductivity background [Eq. (1)].

2. *The general properties of* $\sigma_{xx}(\omega)$

In what follows, we overview the main features of graphene's longitudinal magneto-optical conductivity, an essential step to understand the Faraday rotation in graphene (Sec. III).

Low electronic density.—At low electronic density, more precisely, for $|E_F| < E_1$, no intraband transitions can take place. Because the LLs energy scale in graphene is relative high (e.g., $E_1 \simeq 36$meV for a field of 1 T), the magneto-optical conductivity is fully driven by interband transitions even close to room temperature.

Figure 4 shows a plot of Eq. (42) for zero Fermi energy and a magnetic field of 7T: a sequence of absorption peaks, corresponding to the maximum of the real part of each term in Eq. (39), $\hbar\omega \simeq E_1$, $E_2 - E_{-1}$, $E_3 - E_{-2}$, etc., is clearly observed [see Eq. (49) and text therein]. The conductivity never vanishes even tough the concentrations of carriers is very small ($E_F \to 0$), a genuine signature of graphene's LL structure.[5]

The contributions from different interband transitions [Eq. (39)] partially overlap at high frequency, with the effect that the real part of $\sigma_{xx}(\omega)$ displays the so-called Shubnikov–de Haas oscillations around the universal ac optical conductivity of graphene, σ_g (the imaginary part, in turn, oscillates around zero).[8–15] The semi-classical conductivity is null, on the other hand, thus failing to describe the magneto-transport in neutral graphene.

High electronic density.—Away from charge neutrality, more precisely, for $|E_F| > E_1$, the picture is more involved; intraband transitions can now occur, while some interband transitions will be blocked. We take $T = 0$ and, without loss of generality, assume that $E_F > 0$ (similar conclusions hold for holes); direct inspection of Eq. (41) shows that a single type of intraband transition is allowed, whose contribution to the optical conductivity reads

$$\sigma_{xx}^{\rm intra}(\omega) = \frac{e^2}{h}\frac{2i\hbar v_F^2}{\Delta\omega_{N_F} l_B^2}\frac{\hbar\omega + i\Gamma}{(\hbar\omega + i\Gamma)^2 - \hbar^2\Delta\omega_{N_F}^2}. \quad (44)$$

In the above formula,

$$\Delta_{N_F} \equiv \hbar\Delta\omega_{N_F} = E_{N_F+1} - E_{N_F}\,, \quad (45)$$

denotes the intraband gap, with N_F being the index for the last occupied LL.

Let us first consider the limiting case when the energy gap Δ_{N_F} is larger than the level broadening, $\Delta_{N_F} \gtrsim \Gamma$. The latter typically happens at high magnetic fields and not too high Fermi energies; in this limit, the real part of Eq. (44) displays a maximum at $\omega \simeq \Delta\omega_{N_F}$, with an intensity falling off as $B/\Delta\omega_{N_F}$,

$$\mathrm{Re}\,\sigma_{xx}^{\rm intra}(\Delta\omega_{N_F}) \simeq \left(\frac{2eBv_F^2}{\pi\Gamma\Delta\omega_{N_F}}\right) \times \sigma_g\,. \quad (46)$$

The intraband magneto-peak, Eq. (46), is the lowest frequency peak in the absorption spectrum of graphene with $E_F > E_1$; its magnitude increases with increasing Fermi energy and/or magnetic field intensity. An example of an intraband absorption line occurring at $\omega \simeq \Delta\omega_{N_F}$ can be seen in Fig. 5. In that case, the parameters correspond to $\Delta_{N_F} = 22.6$ meV and $\Gamma = 6.8$ meV, and hence $\Delta_{N_F} \gtrsim \Gamma$. Some points are worth mention: i) the intraband contribution to the conductivity [Eq. (44)] dominates at low photon frequencies; ii) the curve for $\mathrm{Re}\,\sigma_{xx}(\omega)$ shows that the remaining absorption peaks are found in the higher frequency part of the spectrum, above the threshold for interband transitions, $\hbar\omega \geq E_{N_F} + E_{N_F+1}$. (Note that, at low magnetic field and/or high Fermi energy, the level spacing between adjacent LLs is so reduced that $E_{N_F} \simeq E_{N_F+1} \simeq E_F$, and thus one recovers the condition found earlier, namely $\hbar\omega > 2E_F$.) Such interband peaks cause Shubnikov–de Haas oscillations despite the finite electronic density.

For a general relation between the broadening and the energy gap Δ_{N_F}, the maximum for the intraband peak occurs at

$$\omega_{\rm peak}^{\rm intra} = \mathrm{Re}\sqrt{2\Delta\omega_{N_F}\sqrt{\Delta\omega_{N_F}^2 + \Gamma^2/\hbar^2} - \Delta\omega_{N_F}^2 - \Gamma^2/\hbar^2}\,. \quad (47)$$

When $\Delta\omega_{N_F} \leq \Gamma/(\sqrt{3}\hbar)$ (typically the case of very high Fermi energy and/or low magnetic field), the intraband conductivity is maximal at null frequency, with an intensity given by Eq. (46) multiplied by a factor of two.

The regime $\Delta_{N_F} \lesssim \Gamma$ is illustrated in the bottom panel of Fig. 12. Two magnetic fields are considered, at fixed Fermi energy, $E_F = 0.3$eV, with $\mathrm{Re}\,\sigma_{xx}(\omega)$ being represented by the solid lines. When $B = 7$T (left-hand side panel), although a considerable number of levels are occupied ($N_F = 9$), one has $\Delta_{N_F} \simeq 1.4\Gamma$, which, according to Eq. (47), corresponds to a maximum of the longitudinal conductivity at $\omega \simeq \Delta\omega_{N_F}$. This is indeed confirmed

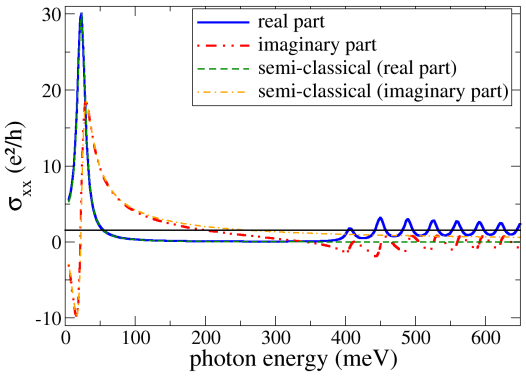

Figure 5: The longitudinal conductivity as function of the photon energy for $E_F = 0.2$ eV. Other parameters as in Fig. 4. The horizontal dashed-dot (black) line marks the graphene's universal ac-conductivity background [Eq. (1)].

by the numerical calculation there shown. Decreasing the magnetic field down to B =3T (right-hand side panel), reduces Δ_{N_F} (recall that LL energy varies as $l_B^{-1} \sim \sqrt{B}$), which in turn increases the number of occupied levels to $N_F = 22$. As a consequence, $\Delta_{N_F} \simeq 0.67\Gamma$, and the maximum of the intraband peak is seen to be shifted to zero frequency, again in accordance with Eq. (47).

Given the intrinsic large cyclotron gap of graphene, E_1, the intraband contribution [Eq. (44)] controls the magneto-optical response of this material in the microwave region up to THz frequencies in samples with finite electronic density ($E_F > E_1$).

The interband contribution, on the other hand, is important both in samples with low electronic density, $E_F < E_1$, where it determines the full magneto-optical response (discarding the effect of phonons as discussed above), and in samples with arbitrary carriers concentrations, for photon energies above the threshold for interband transitions, $\hbar\omega = E_{N_F} + E_{N_F+1}$ (typically within the near infrared region).

The positions of each interband peak can be obtained from Eq. (47), with $\Delta\omega_{N_F}$ replaced by

$$\Delta\Omega_n = (E_{n+1} + E_n)/\hbar\,, \tag{48}$$

with the constraint $n \geq N_F$. At finite electronic densities, $N_F \geq 1$, typically one has $\hbar\Delta\Omega_n \gtrsim \Gamma$, and thus we arrive at the following useful approximation

$$\omega_{\rm peak}^{{\rm inter}\,(n)} \simeq \Delta\Omega_n \quad , n \geq N_F\,. \tag{49}$$

For not too small fields, $B \gtrsim 0.1$T, the cyclotron gap $E_1 \simeq 36 \times \sqrt{B}$ meV$\cdot$T$^{-1/2}$ is larger than the LL broadening, and thus, in practice, the latter statement can be generalized to include the case of $N_F = 0$.

For general parameters, the intensity of each interband peak is no longer given by a simple expression, because many interband transitions can contribute to the spectral weight close to each of the resonances $\omega \simeq \Delta\Omega_n$. As a result, as ω varies, the real part of $\sigma_{xx}(\omega)$ oscillates around a constant value of about $\sigma_{\rm g}$. Examples are shown in Fig. 4 for $E_F = 0$ and in Fig. 5 for $E_F = 0.2$eV. In the first case, we have $N_F = 0$ and therefore all the observed peaks are interband-like. The second case has $N_F = 4$ and therefore one intraband peak is observed, corresponding to transitions $n = 4 \to n = 5$, at low photon energy, whereas the interband peaks appear at energies $\hbar\omega \gtrsim 2E_F = 0.4$eV.

We finally remark that, as long as not too small magnetic fields are considered ($B \lesssim 0.1$ T), the above considerations are valid even close to room temperature (e.g., for $B = 1$T, the first LL corresponds to a thermal energy of 420K).

3. *The Hall conductivity*

The Hall optical conductivity of graphene, $\sigma_{xy}(\omega)$, follows directly from Eq. (7); choosing $i = y$, $j = x$, we obtain

$$\sigma_{xy}(\omega) = -g_s g_v \times \frac{\tilde{J}_y(\omega)}{\tilde{E}_x(\omega)}\,, \tag{50}$$

where we have invoked graphene's six-fold crystallographic symmetry to write $\sigma_{xy}(\omega) = -\sigma_{yx}(\omega)$. The central quantity to be computed this time is the average value of the current density operator along the y direction; using Eqs. (6) and (25), we get

$$J_y(t) = -ev_F \sum_{n,n'} \langle n, k_y | j_y | n', k_y \rangle \langle \hat{c}^\dagger_{n,k_y}(t) \hat{c}_{n',k'_y}(t) \rangle\,. \tag{51}$$

The non-zero matrix elements read

$$\langle 0, k_y | j_y | \pm 1, k_y \rangle = -\,i\frac{ev_F}{\sqrt{2}A}\,, \tag{52}$$

$$\langle n, k_y | j_y | n', k_y \rangle = -\,\frac{ev_F}{2A}\left[{\rm sign}(n')\delta_{|n|-1,|n'|} + {\rm sign}(n)\delta_{|n|,|n'|-1}\right]\,, \tag{53}$$

(plus respective complex conjugates) where, in the last line, $n, n' \neq 0$. Omitting the summation over k_y, the total current density reads

$$\begin{aligned}\hat{J}_y(t) = {} & \frac{i}{\sqrt{2}A} ev_F \left(c_1^\dagger a_0 + v_1^\dagger a_0 - {\rm h.c.}\right) \\ & - \frac{1}{2A} ev_F \sum_{n\geq 1} \left(\hat{P}_n^{(1)} - \hat{P}_n^{(2)} + {\rm h.c.}\right) \\ & - \frac{1}{2A} ev_F \sum_{n\geq 1} \left(c_n^\dagger c_{n+1} - v_n^\dagger v_{n+1} + {\rm h.c.}\right)\,.\end{aligned} \tag{54}$$

The EOMs resemble those derived for the longitudinal conductivity [Eqs. (34)-(35)], the reason being that the current matrix elements in the x and y directions are the

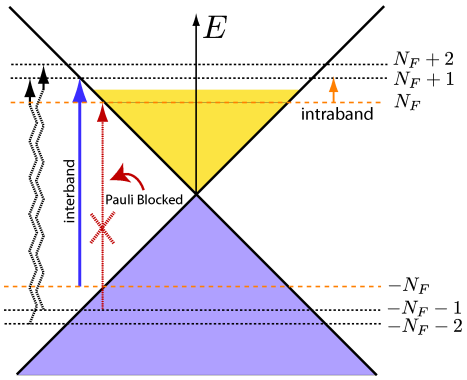

Figure 6: Schematic of electronic transitions contributing to the Hall conductivity of doped graphene in a magnetic field. Contrary to the longitudinal conductivity (Fig. 3), symmetry implies that only interband transitions involving the smallest energy difference, $\hbar\Delta\Omega_{N_F} = E_{N_F} + E_{N_F+1}$, contribute to σ_{xy}. The remaining interband transitions ($\Delta\Omega_n$, with $n > N_F$) come in pairs whose contribution to the Hall current mutually cancel as explained in the text: an example of a pair of interband transitions that cancel is shown in zig-zag arrows. Note: the schematic picture is strictly adequate for $N_F \geq 1$; the case of $N_F = 0$ admits a single type of electronic transition, namely, $n = 0 \to n = 1$.

same expect for phase factors [compare Eqs. (27)-(28) with Eqs. (52)-(53)]. The final formula (after regularization) yields,

$$\sigma_{xy}^{\rm reg}(\omega) = \frac{e^2}{h} \sum_{n\neq m=-N_c}^{N_c} \frac{\Lambda_{nm}^{xy}}{iE_{nm}} \frac{n_F(E_n) - n_F(E_m)}{\hbar\omega + E_{nm} + i\Gamma}\,, \quad (55)$$

with matrix elements Λ_{mn}^{xy} related to Λ_{nm}^{xx} [Eq. (42)] according to,

$$\Lambda_{nm}^{xy} = i\Lambda_{nm}^{xx}(\delta_{|m|,|n|-1} - \delta_{|m|-1,|n|})\,. \quad (56)$$

Likewise $\sigma_{xx}(\omega)$, the result for the Hall conductivity based on the EOM method coincides with the result obtained using Green functions calculations.[42]

Symmetry considerations imply that only two terms contribute in general for the zero-temperature Hall conductivity, and hence the formula Eq. (55) can be considerably simplified. The first term is the intraband contribution and reads,

$$\sigma_{xy}^{\rm intra}(\omega) = \frac{e^2}{h} \frac{2\hbar^2 v_F^2}{l_B^2} \frac{1-\delta_{N_F,0}}{(\hbar\omega + i\Gamma)^2 - \hbar^2\Delta\omega_{N_F}^2}\,, \quad (57)$$

and the second is interband-like, connecting electronic states with $n = -N_F$ and $n = N_F + 1$, and reads,

$$\sigma_{xy}^{\rm inter}(\omega) = \frac{e^2}{h} \frac{2\hbar^2 v_F^2}{l_B^2} \frac{1+\delta_{N_F,0}}{(\hbar\omega + i\Gamma)^2 - \hbar^2\Delta\Omega_{N_F}^2}\,. \quad (58)$$

A single interband transition play a role in setting the Hall conductivity, even for zero Fermi energy. This is at odds with the situation for $\sigma_{xx}(\omega)$, where many non equivalent interband transitions contribute to the optical spectral weight. To understand this peculiar feature of $\sigma_{xy}(\omega)$, let us consider the second lowest interband resonant energy, namely, $\Delta E_2 = E_{N_F+2} - E_{-N_F-1}$: there are two distinct sorts of interband transitions $n \to m$ involving such energy difference, namely, the pair $n_1 = -N_F-2 \wedge m_1 = N_F+1$ and $n_2 = -N_F-1 \wedge m_2 = N_F+2$, whose Hall matrix elements read, $\Lambda_{n_1m_1}^{xy} = i\Lambda_{n_1m_1}^{xx}$ and $\Lambda_{n_2m_2}^{xy} = -i\Lambda_{n_2m_2}^{xx}$, respectively. When substituting into Eq. (55), these contributions cancel each other at $T = 0$ because $\Lambda_{n_2m_2}^{xx} = \Lambda_{n_1m_1}^{xx}$. The same argument applies to all transitions involving an energy difference larger than the interband gap, $\hbar\Delta\Omega_{N_F}$. The only exception is indeed the interband transition $-N_F \to N_F + 1$ because, contrary to interband transitions involving larger energy differences, it cannot be canceled by the other member of the pair, $n = -N_F - 1 \wedge m = N_F$, since the latter is forbidden via Pauli blockade; a schematic picture is given in Fig. 6.

The extrema points of the real part of the Hall conductivity occurs at zero frequency, $\omega = 0$, and

$$\omega_\pm^{\rm intra} \simeq \Delta\omega_{N_F} \pm \Gamma/\hbar\,, \quad (59)$$

$$\omega_\pm^{\rm inter} \simeq \Delta\Omega_{N_F} \pm \Gamma/\hbar\,, \quad (60)$$

where we have considered $\Gamma/\hbar \lesssim \Delta\omega_{N_F}$ [see Eq. (46) and text therein] and made use of $\Gamma/\hbar \ll \Delta\Omega_{N_F}$. The latter consideration is true virtually in all situations except for graphene at low electronic density and small magnetic field B. Within the same accuracy, the Hall conductivity at $\omega = 0$ reads

$$\mathrm{Re}\,\sigma_{xy}(0) \simeq -\left(\frac{1-\delta_{N_F,0}}{\Delta\omega_{N_F}^2} + \frac{1+\delta_{N_F,0}}{\Delta\Omega_{N_F}^2}\right)\left(\frac{4eBv_F^2}{\hbar\pi}\right)\times\sigma_{\rm g}\,, \quad (61)$$

whereas at the point $\omega_\pm^{\rm intra}$ is given by

$$\mathrm{Re}\,\sigma_{xy}(\omega_\pm^{\rm intra}) = \simeq F_{\Delta\omega_{N_F}}^\pm \left(\frac{1-\delta_{N_F,0}}{\Delta\omega_{N_F}}\right)\left(\frac{eBv_F^2}{\pi\Gamma}\right)\times\sigma_{\rm g}\,, \quad (62)$$

and for $\omega_\pm^{\rm inter}$ reads

$$\mathrm{Re}\,\sigma_{xy}(\omega_\pm^{\rm inter}) \simeq F_{\Delta\Omega_{N_F}}^\pm \left(\frac{1+\delta_{N_F,0}}{\Delta\Omega_{N_F}}\right)\left(\frac{eBv_F^2}{\pi\Gamma}\right)\times\sigma_{\rm g}\,, \quad (63)$$

where we have defined $F_\omega^\pm = \pm\hbar\omega/(\hbar\omega \pm \Gamma)$. The intensity of the Hall peaks dependence on the magnetic field intensity B is the same than for the longitudinal (intraband) peaks [Eq. (46)], i.e., as $\sim\sqrt{B}$. Also, similarly to $\sigma_{xx}(\omega)$, in doped graphene with $N_F > 1$, the interband peak is very low when compared to the intraband Hall peak for $\Delta\omega_{N_F} \ll \Delta\Omega_{N_F}$. We finally remark that the anomaly associated to the zero energy LL is present in all the latter expressions via the factor $1 + \delta_{N_F,0}$.

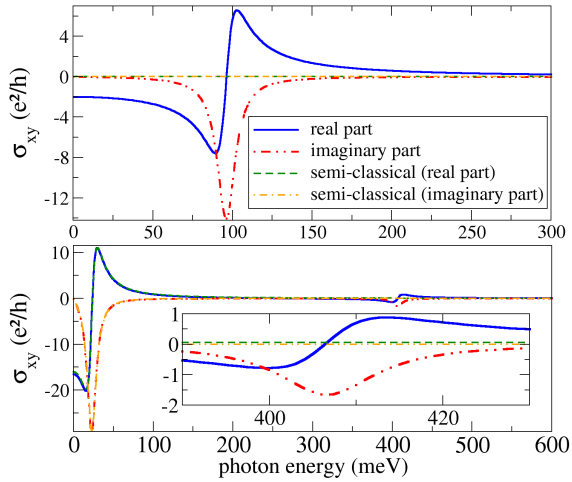

Figure 7: Hall conductivity as function of photon energy for $E_F = 0$ (top panel) and $E_F = 0.2$ eV (bottom panel). In both plots $T = 0$ (other parameters as in Fig. 4). At zero Fermi energy (top), $\sigma_{xy}(\omega)$ originates in a single type of interband transition, centered at $\hbar\omega \approx E_1 \simeq 96$ meV, and therefore cannot be described by a semi-classical treatment [Eq. (58)]. When $E_F = 0.2$ eV (bottom), we have the first four LLs fulfilled, which results in a classical intraband contribution [Eq. (57)], centered at $\hbar\omega \simeq E_5 - E_4 \approx 23$ meV, and a single interband transition [Eq. (58)] centered at $\hbar\omega \simeq E_5 + E_4 \approx 0.4$ eV $\simeq 2E_F$. The latter is shown in the inset.

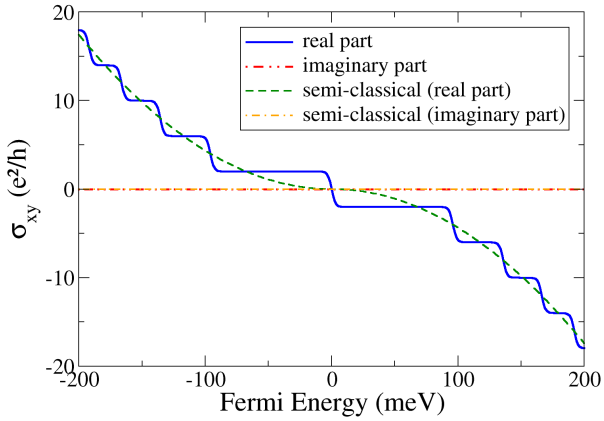

Figure 8: The dc Hall conductivity as function of the Fermi energy. The parameters are $T = 17$ K and $\Gamma = 0.68$ meV. The plateaux show Hall quantization values according to the theoretical prediction for massless Dirac fermions [Eq. (64)].

Figure 7 shows the Hall conductivity of graphene at high magnetic field ($B = 7$ T) for $N_F = 0$ (top panel) and $N_F = 4$ (bottom panel), corresponding to neutral and highly doped graphene samples, respectively. The main characteristics of $\mathrm{Re}\,\sigma_{xy}(\omega)$ can be explained using Eqs. (61)-(63). In particular, for doped graphene, the spectral weight concentrates around two well separated parts of the spectrum: i) an intraband dominated region ($n = 4 \to n = 5$), at low photon energies, with maximum (minimum) intensity occurring at $\hbar\omega_+ \simeq \Delta_4 + \Gamma \simeq 30$ meV ($\hbar\omega_- \simeq \Delta_4 - \Gamma \simeq 16$ meV) [intensity equal to $\simeq 10e^2/h$ ($\simeq -20e^2/h$), in accordance with Eq. (62)], and ii) an interband dominated region $n = -4 \to n = 5$, at high photon energies, with maximum (minimum) intensity occurring at $\hbar\Omega_+ \simeq \hbar\Delta\Omega_4 + \Gamma \simeq 413$ meV ($\hbar\Omega_- \simeq \hbar\Delta\Omega_4 - \Gamma \simeq 400$ meV) [intensity equal to $\simeq 0.81e^2/h$ ($\simeq -0.85e^2/h$), in accordance with Eq. (63)].

Dependence on the Fermi energy.— The variation of conductivity with the Fermi energy reveals other peculiar feature of 2D systems: the Hall quantization.[26,30] Figure 8 shows the formation of plateau in the static (or dc) Hall conductivity, $\sigma_{xy}(0)$, a direct evidence for discrete energy levels. In conventional 2D electron gases, the widths of such plateau are constant (the LLs energy scales as n), whereas in graphene the plateau's width decreases with increasing Fermi energy (the LLs energy scales as $\sqrt{n}$). As for the steps heights, they are equidistant in graphene, $\Delta\sigma_{xy}(0) = 4e^2/h$, even when crossing $E_F = 0$, whereas in conventional 2D systems the step from the first electron LL ($n = 1$) and the first hole LL ($n = -1$) is twice the value of the remaining steps (a manifestation of the zero-energy LL graphene anomaly).

The Hall conductivity quantization rule of graphene can be readily obtained adding the intraband and interband Hall conductivities,

$$\sigma_{xy}(0) = -\frac{4e^2}{h}\left(N_F + \frac{1}{2}\right), \qquad (64)$$

where we have used $\Gamma \ll E_1$ in order to simplify the denominators of Eqs. (57)-(58). Despite the filling factor, $\nu = 4N_F + 2$, being an integer number, there is no complete correspondence with the conventional 2D integer quantum Hall effect, for which $\sigma_{xy} = -4e^2N_F/h$; an extra 1/2 factor due to the contribution of the zero energy state, shared by both electrons and holes, shows up which must be taken separately, making ν always even—this is known as the *anomalous* IQHE and is a hallmark of chiral massless fermions. The anomalous IQHE was predicted theoretically[8,41] and measured[5,27] in the yearly days of graphene.

E. The semi-classical solution

Within the semiclassical approach, the spinorial nature of the electrons' wave function is immaterial. On the other hand, the massless nature of the spectrum invalidates a straightforward Drude-like approach[44,45] to the calculation of the transport coefficients, and Boltzmann transport theory is required, since in this formulation the central quantity to be computed is the deviation of the momentum distribution function from the equilibrium Fermi distribution.

In the semi-classical regime (that is high electronic density and/or low magnetic fields), the physics of the Hall effect can be explained in terms of Boltzmann's theory of transport, where the electric current is given, in the case of graphene, by:

$$\boldsymbol{J} = \frac{e^2}{h}\int d\mathbf{k} g(B,\mathbf{k},\omega)\boldsymbol{v}_{\mathbf{k}}\,, \tag{65}$$

with spin and valley degeneracies included, and where $g(B,\mathbf{k},\omega) \equiv g_{\mathbf{k}}$, is the deviation of the carriers' (electrons or holes) distribution function from the equilibrium Fermi distribution, $f_0(\epsilon)$, e is the charge of the carrier, the static magnetic field B is considered to be perpendicular to graphene's surface, ω is the frequency of the electromagnetic field, and the carrier's velocity reads $\boldsymbol{v}_{\mathbf{k}} = (v_x, v_y) = v_F(\cos\theta, \sin\theta)$. In the presence of both a electric and a magnetic field, the distribution $g_{\mathbf{k}}$ is the solution of the following equation[44]

$$-e\mathbf{E}\cdot\boldsymbol{v}_{\mathbf{k}}\frac{\partial f_0}{\partial\epsilon} = \frac{g_{\mathbf{k}}}{\tau_{\mathbf{k}}} + \frac{\partial g_{\mathbf{k}}}{\partial t} + \frac{e}{\hbar}\left(\boldsymbol{v}_{\mathbf{k}}\times\mathbf{B}\right)\cdot\nabla_{\mathbf{k}} g_{\mathbf{k}}\,, \tag{66}$$

where we have employed the the standard relaxation approximation[44], i.e.,

$$\left.\frac{\partial f_{\mathbf{k}}}{\partial t}\right|_{\rm scatt} = -\frac{g_{\mathbf{k}}}{\tau_{\mathbf{k}}}\,, \tag{67}$$

with $\tau_{\mathbf{k}}$ the relaxation scattering time, $\mathbf{E} = (E_{0,x}, E_{0,y})$ is the electric field, and $\nabla_{\mathbf{k}}$ is the gradient operator with respect to the momentum $\mathbf{k}$. Writing $g_{\mathbf{k}}$ as,

$$g_{\mathbf{k}} = e^{-i\omega t}\mathbf{k}\cdot\mathbf{A}\,, \tag{68}$$

and noting that $(\boldsymbol{v}_{\mathbf{k}}\times\mathbf{B})\cdot\nabla_{\mathbf{k}} g_{\mathbf{k}} = \boldsymbol{v}_{\mathbf{k}}\cdot(\mathbf{B}\times\nabla_{\mathbf{k}} g_{\mathbf{k}})$, Eq. (66) can be solved exactly, where the vector $\mathbf{A}$ needs to be determined. Solving Eq. (66), the components of the vector $A = (A_x, A_y)$ are obtained in the form

$$A_x = \frac{(1-i\omega\tau_{\mathbf{k}})E_x - \tau_{\mathbf{k}}\omega_c E_y}{(1-i\omega\tau_{\mathbf{k}})^2 + \omega_c^2\tau_{\mathbf{k}}^2}\,, \tag{69}$$

$$A_y = \frac{(1-i\omega\tau_{\mathbf{k}})E_y + \tau_{\mathbf{k}}\omega_c E_x}{(1-i\omega\tau_{\mathbf{k}})^2 + \omega_c^2\tau_{\mathbf{k}}^2}\,, \tag{70}$$

where

$$\omega_c = ev_F^2 B/|E_F|\,, \tag{71}$$

is the graphene's cyclotron frequency, and $E_{x(y)}$ is defined as

$$E_{x(y)} = -eE_{0,x(y)}v_{x(y)}\frac{\partial f_0}{\partial\epsilon}\,. \tag{72}$$

Introducing $g_{\mathbf{k}}$ in Eq. (65), and assuming $T = 0$, we obtain the components of the conductivity tensor, which read

$$\sigma_{xx} = \frac{e^2}{h}\frac{2|E_F|\tau_{k_F}}{\hbar}\frac{1-i\omega\tau_{k_F}}{(1-i\omega\tau_{k_F})^2+\omega_c^2\tau_{k_F}^2}\,, \tag{73}$$

$$\sigma_{xy} = -\frac{e^2}{h}\frac{2E_F\tau_{k_F}}{\hbar}\frac{\omega_c\tau_{k_F}}{(1-i\omega\tau_{k_F})^2+\omega_c^2\tau_{k_F}^2}\,, \tag{74}$$

Remark that setting $\omega_c = 0$ in Eq. (73) leads to the semi-classical longitudinal conductivity at zero field mentioned in Sec. II C.

The validity of the semi-classical calculation.—The results presented so far demonstrate the reliability of the Boltzmann approach in the regions of the spectrum where the optical weight is mostly due to intraband transitions. This is borne out in Fig. 5 [Fig. 7 (bottom panel)], where $\sigma_{xx}(\omega)$ [$\sigma_{xy}(\omega)$] is plotted as function of $\hbar\omega$, for $B = 7$ T and $E_F = 0.2$ eV: the agreement between the real part (imaginary part) of the quantum calculation shown in blue line (dashed double dot line) and the semi-classical calculation shown in dashed curve (dashed-dot line) in these figures is confined to energies $\hbar\omega \lesssim 2E_F$. For high photon frequencies, more precisely, above the threshold for interband transitions, $\hbar\omega \simeq 2E_F$, the conductivity cannot be described by Boltzmann's transport theory.

The fine agreement observed at low photon energies is not accidental and only ceases to happen for very small Fermi energy. To see why, we note that Eqs. (44) and (57) (intraband conductivity) and Eqs. (73)-(74) (semi-classical conductivity) coincide upon identification of the intraband energy gap Δ_{N_F} with the cyclotron energy, $\hbar\omega_c$. This identification is justified when a sufficient number of LLs are filled. In fact, expressing the Fermi energy as $E_F = (\hbar v_F/l_B)\sqrt{2N^\star}$, we obtain $\Delta_{N_F} \to \hbar\omega_c$ provided that

$$\sqrt{N_F+1} - \sqrt{N_F} \to \frac{1}{2\sqrt{N^\star}}\,. \tag{75}$$

Noting that $N_F = \mathrm{int}[N^\star]$, we then see that latter limit is achieved when $N^\star \gg 1$, as anticipated.

For the parameters in Fig. 5 [see also Fig. 7 (bottom panel)], even though only a few LLs are fulfilled, i.e., $N_F = 4$, the values of Δ_{N_F} and $\hbar\omega_c$ are quite similar, $\Delta_{N_F} = 0.0226$ eV and $\hbar\omega_c = 0.0230$ eV, explaining the consistence between both theories in describing the intraband electronic transport. In practice, only for very small Fermi energy and/or very high magnetic field, such that $N_F = 0$, the semi-classical calculation fails to describe the conductivity in the whole optical spectrum, since all transitions are interband-like in such case. Remarkably, already for a single LL occupied, $N_F = 1$, the semi-classical calculation provides a reasonable description of the optical conductivity, as long as one keeps inside the portion of the spectrum where the interband processes have little or none weight, that is, $\hbar\omega \lesssim E_1 + E_2$ (see Fig. 9). We note again, however, that the intraband region extends for a large range of frequencies given the large intrinsic cyclotron gap of graphene.

In summary, the validity of the semi-classical calculation is bounded to photon energies below the interband threshold, $\hbar\omega \lesssim E_{N_F} + E_{N_F+1}$, and for not too small Fermi energy, $N_F \gtrsim 1$. For the parameters used in Figs. 5, 7 (bottom panel), 9 and 11, we list in Table I the corresponding values of $\Delta_{N_F}/\hbar\omega_c$. Those figures have $N_F > 1$ and hence the semi-classical conductivity agrees well within the far infrared part of the spec-

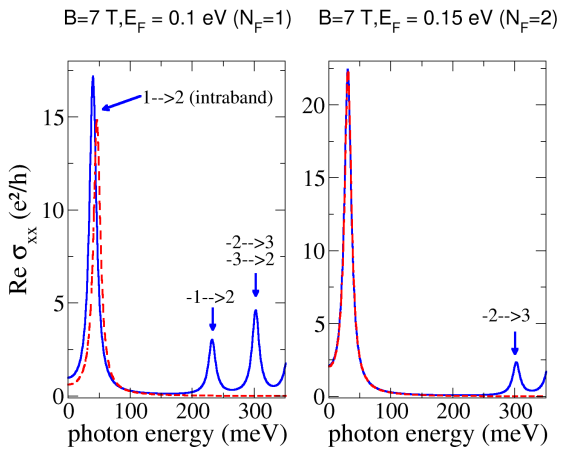

Figure 9: The real part of the longitudinal conductivity is plotted as function of the photon energy for $E_F = 0.1$ eV (left panel) and $E_F = 0.15$ eV (right panel). In these plots, $B = 7$ T and $\Gamma = 6.8$ meV. The red dashed line stands for the semi-classical result [Eq. (73)] and the blue solid line represents the EOM quantum solution [Eq. (42)]. Remark that, in the right panel, there is no interband peak $n = -1 \to m = 2$, at $E_F \approx 230$ meV, and the peak at $\hbar\omega \approx 300$ meV looses halve of its intensity because the $n = -3 \to m = 2$ transitions get blocked when the Fermi energy crosses the LL with $n = 2$.

trum. For completeness, Fig. 9 shows the real part of $\sigma_{xx}(\omega)$ for $N_F = 1$ (left panel) and $N_F = 2$ (right panel). The former has $\Delta_{N_F}/\hbar\omega_c \simeq 0.86$ and hence the semi-classical calculation is only partially accurate. In particular, it underestimates the maximum intensity for intraband light absorption. The panel with $N_F = 2$ has $\Delta_{N_F}/\hbar\omega_c \simeq 0.99$, which explains the excellent agreement between both curves in the intraband region, $\hbar\omega \lesssim 0.3$ eV.

B (T)	E_F (eV)	N_F	$\Delta_{N_F}/\hbar\omega_c$
1	0.30	68	0.9990
2	0.30	34	0.9954
5	0.30	13	1.0066
7	0.20	4	0.9837
7	0.15	2	0.9933
7	0.10	1	0.8629

Table I: Values of several relevant quantities related to the numerical simulations given in Figs. 5,7,9 and 11. The agreement between the semi-classical calculation and the quantum intraband expression comes from the similarity between Δ_{N_F} and $\hbar\omega_c$.

Having presented the calculation method of the magneto-optical properties of graphene based on the equation of motion method, we we now turn to the study of the Faraday effect.

III. THE FARADAY EFFECT IN GRAPHENE

We want to discuss the transmission of electromagnetic radiation between two dielectric media separated by graphene. The scattering geometry is given in Fig. 10, where the transverse magnetic mode was chosen as a particular example. Since we will be interested in normal incidence, there is no distinction between the transverse magnetic and the transverse electric modes.

The present section is organized as follows: in Sec. III A, we derive general expressions for transmission, ellipticity and Faraday rotation angle. These quantities depend on the frequency of the impinging light, ω, magnitude of (transverse) magnetic field, B, scattering mechanisms (i.e., level broadening, Γ), temperature, T, and Fermi energy, E_F, via the magneto-optical conductivity tensor of graphene derived in Sec. II.

Our theoretical results are tested against experimental data measured recently by Crassee *et al.* using graphene samples with large electronic density.[33] The limit of low electronic density is studied in Sec. III C, where the Faraday rotation angle is shown to display quantum jumps as a function of the Fermi energy.

Finally, in Sec. III D, an experimental setup is proposed that is able to greatly enhance the Faraday rotation angle in the entire optical spectrum.

A. Faraday rotation in graphene

We now solve the problem posed in Fig. 10, considering only a single graphene sheet separating two dielectrics. In what follows, we assume that graphene is deposited on top of lossless dielectric medium (that is fully transparent to the impinging light), of relative permittivity ϵ_r. The generalization of the problem to the case of a lossy dielectric poses no difficulties, except for the introduction of a complex index of refraction associated with the dielectric medium. We further assume that the incoming electromagnetic field is linearly polarized along the x-axis and propagates along the z-direction, as shown in the diagram of Fig. 10, that is

$$\boldsymbol{E}^i = \mathbf{e_x} E_x^i e^{i(qz-\omega t)}\,, \tag{76}$$

such that $q = \sqrt{\epsilon_r}\omega/c$.

Due to the optical Faraday rotation of the plane of polarization of the electric field, both the reflected, $\boldsymbol{E}^r$, and the transmitted, $\boldsymbol{E}^t$, fields acquire a finite component along the y-direction, that is

$$\boldsymbol{E}^r = (E_x^r, E_y^r) e^{-i(qz-\omega t)}\,, \tag{77}$$

$$\boldsymbol{E}^t = (E_x^t, E_y^t) e^{i(kz-\omega t)}\,, \tag{78}$$

where $k = \omega/c$. For this problem, Maxwell's equations for the electric field reads (in MKS units)

$$\frac{\partial^2 E_i}{\partial z^2} + i\omega\mu_0\delta(z)\sum_{j=x,y}\sigma_{ij}E_j + \omega^2\epsilon_r\mu E_i = 0\,, \tag{79}$$

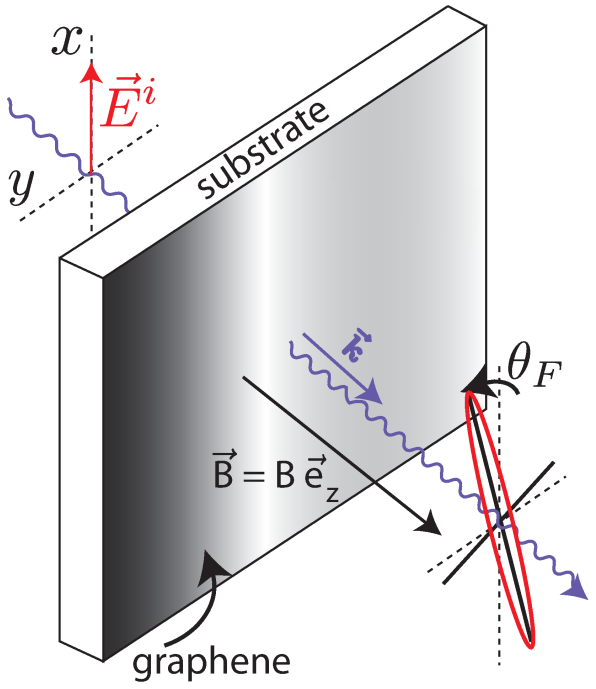

Figure 10: Schematic of the Faraday effect: an electromagnetic wave polarized in the xy plane (transverse magnetic mode) and traveling in the positive z direction passes through a graphene film subjected to a transverse magnetic field B. In this case, graphene is adhered to a substrate (typically SiO_2), but the experiment can also be made with suspended graphene. The transmitted field sees its plane of polarization rotated by an angle θ_F and acquires a certain degree of ellipticity.

where E_i is the i-component of the electric field (we have $i = x, y$), μ_0 is the vacuum permeability, and σ_{ij} are the components of the magneto-optical tensor of graphene (see Sec. II). The boundary conditions at the substrate-graphene-air interface are the continuity of the tangential components of the electric field at the surface of graphene ($z = 0$),

$$\left(E_x^i, 0\right) + \left(E_x^r, E_y^r\right) = \left(E_x^t, E_y^t\right) , \tag{80}$$

and (the derivatives are evaluated at $z = 0$)

$$\frac{\partial E_l^t}{\partial z} - \frac{\partial E_l^i}{\partial z} - \frac{\partial E_l^r}{\partial z} = -i\omega\mu_0 \sum_{j=x,y} \sigma_{lj} E_j^t , \tag{81}$$

where the last condition was derived from integrating Eq. (79) in the interval $z \in [0^-, 0^+]$ and $l = x, y$. The calculation of the transmitted intensities becomes easier to perform if we rewrite the boundary conditions in terms of circularly polarized waves:

$$-2qE_x^i + (k+q)E_\pm^t = -\mu\omega\sigma_\mp E_\pm^t , \tag{82}$$

where $E_\pm = E_x \pm iE_y$ and $\sigma_\pm = \sigma_{xx} \pm i\sigma_{xy}$, for in this representation the two circular polarizations decouple from each other. From Eqs. (82) it follows the transmission amplitudes in the form:

$$t_\pm \equiv \frac{E_\pm^t}{E_x^i} = \frac{2\sqrt{\epsilon_r}}{1 + \sqrt{\epsilon_r} + c\mu_0\sigma_\mp} = |t_\pm| e^{i\theta_\pm} . \tag{83}$$

The transmittance can be written as,

$$T(B) = \frac{1}{2\sqrt{\epsilon_r}} \left(|t_+|^2 + |t_-|^2\right) , \tag{84}$$

where the factor $1/2$ comes from the proper normalization of circularly polarized waves (omitted in the definition above, for simplicity of writing) and the factor $1/\sqrt{\epsilon_r}$ is due to flux conservation. Faraday's rotation angle, θ_F, and the ellipticity are given by[46–48]

$$\theta_F = \frac{1}{2}\left(\theta_+ - \theta_-\right) , \tag{85}$$

$$\delta = \frac{|t_+| - |t_-|}{|t_+| + |t_-|} , \tag{86}$$

respectively. From Eq. (83), θ_F is given in terms of the conductivity $\sigma_\pm$, since

$$\theta_\pm = -\arctan \frac{\mu c \sigma''_\mp}{1 + \sqrt{\epsilon_r} + c\mu\sigma'_\mp} , \tag{87}$$

where $\sigma_\pm = \sigma'_\pm + i\sigma''_\pm$, and $\sigma'_\pm$ and $\sigma''_\pm$ are the real and imaginary parts of $\sigma_\pm$, respectively. Explicitly, we have

$$\sigma_\pm = \left(\sigma'_{xx} \mp \sigma''_{xy}\right) + i\left(\sigma''_{xx} \pm \sigma'_{xy}\right) , \tag{88}$$

from which follows the approximate expression

$$\theta_F \approx -\frac{c\mu_0}{1 + \sqrt{\epsilon_r}} \sigma'_{xy} , \tag{89}$$

where we have assumed that $\theta_F \lesssim 1$ and that $1 + \sqrt{\epsilon_r} \gg c\mu_0\sigma'_\mp$. The last assumption is the more stringent of the two. For comparison, in the numerical studies we give in Fig. 11, we represent both the exact and the approximate results for θ_F, δ, and T. This allow us to check the validity of the approximate results. Discarding terms of the order of $(c\mu_0\sigma_\mp)^2$ in Eq. (84) we obtain an approximate expression for the total transmitted light in the form

$$T(B) \approx \frac{4\sqrt{\epsilon_r}}{(1 + \sqrt{\epsilon_r})^2} \left(1 - \frac{2c\mu_0}{1 + \sqrt{\epsilon_r}} \sigma'_{xx}\right) . \tag{90}$$

Within the same degree of approximation used to derive Eq. 89, the ellipticity is given by

$$\delta \approx -\frac{2c\mu}{1 + \sqrt{\epsilon_r}} \sigma''_{xy} . \tag{91}$$

The validity of these approximations depend on the photon frequency as it can be seen in Fig. 11. In what follows, the exact expression will be used in all numerical studies.

In our simulations of the Faraday effect, we assume broadenings of the order of 10 meV. Our assumption is consistent with the values found in pump-probe experiments performed in exitaxial and exfoliated graphene samples[49,50], and on infrared spectroscopy studies of the Drude conductivity of graphene.[51]

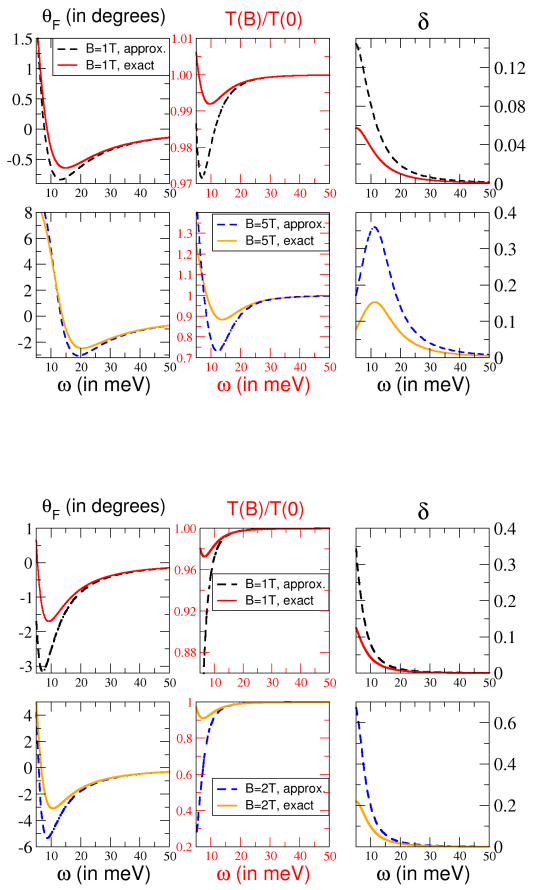

Figure 11: Faraday rotation angle (given in degrees), normalized transmittance, and ellipticity of electromagnetic radiation passing through graphene subjected to a perpendicular magnetic field. The graphene sample is assumed to have a finite electronic density, $E_F = 0.3$ eV, and to be on top of SiO_2 ($\epsilon_r = 3.9$). Top six panels: simulation of θ_F, $T(B)/T(0)$, and δ, considering a broadening of $\Gamma = 7$ meV. Bottom six panels: simulation of the same quantities as above for $\Gamma = 3.7$ meV. In all panels, the dashed lines correspond to approximate calculations, as given by Eqs. (89)-(91), and $T = 17$ K.

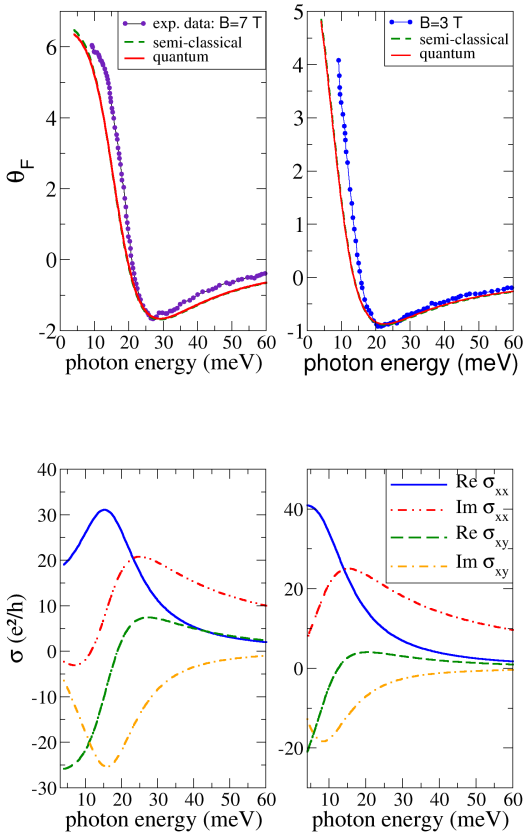

Figure 12: The Faraday effect in doped graphene. **Top**: The Faraday rotation angle (given in degrees) when graphene is grown on silicon carbide. Fit to the experimental values of θ_F, at a magnetic field of $B = 7$ T (left panel) and $B = 3$ T (right panel), using the semiclassical approach (green dashed line) and the full quantum calculation (red solid line). The parameters are: $E_F = 0.3$ eV, $\Gamma = 10.5$ meV, $T = 6$ K and $\epsilon_r = 4.4$. **Bottom**: The theoretical optical conductivity [Eqs. (42) and (55)] for the same parameters used to fit the experimental data: $B = 7$ T (left panel) and $B = 3$ T (right panel).

B. Fit to experimental data in the high-density regime

Fig. 12 shows fits for two sets of experimental data for θ_F[33], measured when electromagnetic radiation passes through graphene epitaxially grown on silicon carbide (data taken at a temperature of 6 K). According to the experiments by Crassee et al. (Ref. 33) it was possible to produce a single graphene sheet grown on the Si-terminated surface of 6H-SiC (the sample underwent H-passivation of the Si dangling bonds, resulting in quasi-free standing single layer graphene). Two sets of experimental data are shown in Fig. 12 (top panel), corresponding to two magnetic field intensities, $B = 7$ T and $B = 3$ T.

In the course of the experiments it was found that the bare substrate did not reveal any Faraday effect, and therefore the measured rotation angle is intrinsic of graphene. This statement is confirmed by the model developed in Sec. III A. ARPES measurements on the used sample indicated a Fermi energy of the order of $E_F \simeq 0.34 \pm 0.01$ eV.

In order to fit the data we have used $E_F = 0.3$ eV. We do not expect a perfect fit because we are considering a lossless dielectric. Nevertheless the fit is fairly accurate, given the simplicity of the model. Moreover, the value of ϵ_r was set to 4.4 which is not the relative permittivity of SiC and must be understood as an effective number, given that the experimental data was taken with epitaxially grown graphene. Although the calculation of Sec. II D

does not include this fact explicitly, the fits are satisfactory for they reproduce the main features of the experimental data: a decrease of θ_F with the photon energy until a minimum is reached for $\hbar\omega \approx 26$ meV (20 meV) when the magnetic field intensity is 7 T (3 T).

Comparing the top and bottom panels of Fig. 12, it can be seen that the minimum (maximum) of the Faraday rotation angle coincides roughly with the maximum (minimum) of σ'_{xy}. The latter fact agrees well with what could be concluded from the approximated result stated in Eq. (89). In order to interpret the variation of the Faraday rotation angle with the photon energy, it is sufficient to use the simplified results derived in Sec. II D for $T = 0$, namely, Eqs. (57)-(63). (This is plainly justified given the low temperature in the experiment of Ref. 33; the respective thermal energy corresponds to about 0.01 times the level spacing $\Delta_1 = E_1 - E_0$ [see Eq. (45) for the definition of Δ_n] for both intensities of magnetic field.)

For a magnetic field of 7 T (3 T), intraband transitions $n = 9 \to n = 10$ ($n = 22 \to n = 23$) control the variation of θ_F, from positive up to negative values, as the photon energy varies. Here, the index n denotes LLs with energy given by $E_n = \mathrm{sign}(n)\sqrt{2|n|}\hbar v_F/l_B$ [see Eq. (5) and text therein]. The remaining transitions contributing to the Hall conductivity are interband-like and occur at much higher photon energies $\hbar\omega \simeq 2E_F$, and thus it does not influence the Faraday rotation in the range of energy plotted in Fig. 12.

In this example, intraband transitions involve a very small difference of energy, even when the magnetic field is 7 T. The value of the intraband gap [Eq. (45)] is $\Delta_{N_F} \simeq 16$ meV ($\Delta_{N_F} \simeq 7$ meV) for $B = 7$ T ($B = 3$ T), which is comparable to Γ (here N_F denotes the last occupied LL for a given Fermi energy). The exact calculation shows that the extrema points of the real part of the intraband Hall conductivity [Eq. (57)] occur at $\omega = 0$, and,

$$\omega_{\pm}^{\mathrm{intra}} = \frac{1}{\hbar}\mathrm{Re}\sqrt{\Delta_{N_F}^2 + \Gamma^2 \pm 2\Gamma\sqrt{\Delta_{N_F}^2 + \Gamma^2}}\,. \qquad (92)$$

Substituting the values given in the caption of Fig. 12 into the latter formula, we obtain $\omega_+^{\mathrm{intra}} \simeq 27$ meV ($\omega_+^{\mathrm{intra}} \simeq 20$ meV) for a field intensity of 7 T (3 T). As above-mentioned, these are the points where the Faraday rotation reaches its minimum value. Increasing further the photon energy, $\hbar\omega > \hbar\omega_+^{\mathrm{intra}}$, the Faraday rotation increases towards zero, essentially because at large ω, below the interband threshold, the Hall conductivity becomes very small (Fig. 12) and no distinction arises between σ_- and σ_+, and thus $t_+ \approx t_-$. Increasing the photon energy up to $\hbar\omega \sim 2E_F$, the interband transition comes into play and drives the Faraday rotation. Interband transitions are important in samples with low electronic densities, as explained in the following section.

The curves for θ_F, computed either from the semi-classical expressions for the conductivity [Eqs. (73)-(74)] or via the EOM expressions [Eqs. (42) and (55)] are almost indistinguishable (see Fig. 12, top panel), in the range of photon energies considered, except for $\hbar\omega \approx$ 10 meV, where a very small deviation is observed when the intensity of the magnetic field is 7 T.

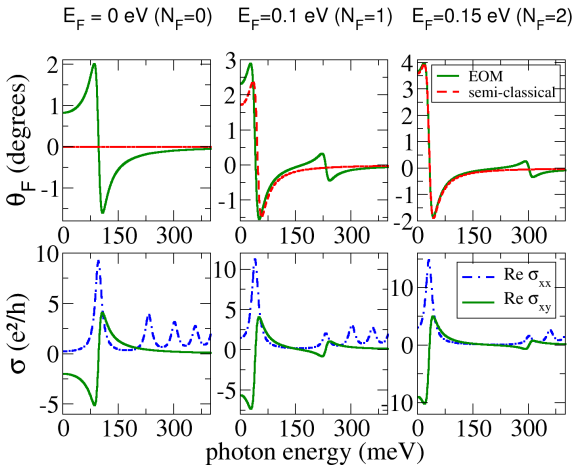

Figure 13: The low electronic density limit. **Top**: Faraday rotation angle (given in degrees) for free-standing graphene ($\epsilon_r = 1$) for different LLs occupations: from left to right, $N_F = 0, 1$ and 2. The magnetic field intensity is $B = 7$ T, $\Gamma = 10.5$ meV and $T = 0$. Adding a dielectric substrate to graphene decreases the maximum amount of Faraday rotation that is achievable, without introducing major qualitative changes (see Eq. 89). **Bottom**: The real part of the quantum conductivity tensor for the Fermi energies considered in the top panel.

The agreement between the quantum and the semi-classical solutions is explained by the similarity of the intraband gap Δ_{N_F} and the cyclotron energy $\hbar\omega_c$ [see Eq. (71)]. The values for these quantities are $\Delta_{N_F} \simeq 6.62(15.6)$ meV and $\hbar\omega_c \simeq 6.58(15.4)$ meV for a field of 3(7) T. The agreement between both methods breaks down near the interband threshold, $\hbar\omega \simeq 2E_F \simeq 0.6$ eV, where the quantum contribution, arising from the interband transition cannot be neglected.

C. Quantum jumps in the Faraday rotation: the low electronic density limit

When small Fermi energies are considered, energy quantization becomes important (see Secs. II D and II E). The limiting case occurs for $0 \leq E_F < \sqrt{2}\hbar v_F/l_B$, i.e., $N_F = 0$. In such case, at $T = 0$, the LLs with $n \geq 1$ are all empty, and a single type of transition contributes to the Hall conductivity, $n = 0 \to n = 1$. Since this transition is interband-like it cannot be explained within the semi-classical treatment (Secs. II D and II E). This situation is illustrated in Fig. 13 (bottom panel): when $N_F = 0$, the real part of the Hall conductivity (solid line) has a finite (non-zero) value around $\omega \simeq (E_1 + E_0)/\hbar$ [note: the extrema of the interband Hall conductivity can be obtained from Eq. (92) making the replacement

$\Delta_{N_F} \to \hbar\Delta\Omega_{N_F}$, with $\Delta\Omega_{N_F}$ given by Eq. (48)]. The Faraday rotation given by the semi-classical model is obviously zero (dashed line) since $E_F = 0$ [Eq. (74)]. The respective Faraday rotation angle (top panel) is approximately proportional to $-\sigma_{xy}(\omega)$.

At higher Fermi energies (i.e., $N_F > 0$), two types of transitions contribute to the Hall conductivity: in general, for $E_{N_F} < E_F < E_{N_F+1}$, with $N_F \geq 1$, the allowed transitions are i) interband between the hole's LLs with $n = -N_F$ and the electron's LLs with $n = N_F + 1$ and, ii) intraband between LLs with $n = N_F$ and $n = N_F + 1$ (Sec. II D). The maximum intensity of σ'_{xy} falls off with the inverse of the energy difference associated with a given electronic transition [Eqs. (62)-(63)]. Since, up to a good degree of approximation, the Faraday effect is controlled by σ'_{xy}, the latter means that the amount of Faraday rotation induced by the interband transitions at $\omega = \Delta\Omega_{N_F}$ will be smaller than the Faraday rotation due to intraband processes.

The above-mentioned facts can be appreciated in Fig. 13, where numerical data for θ_F (top panels), σ'_{xx} and σ'_{xy} (bottom panels) is shown with Fermi energy increasing from the left to the right. As higher LLs in the conduction band become occupied, the spectral weight for the interband contribution to σ'_{xy} shifts towards higher energies (that is, $\hbar\Delta\Omega_{N_F}$ increases $\to \omega_{\pm}^{\rm inter}$ increases). The opposite occurs for the intraband transitions, since in this case, the relevant energy scale Δ_{N_F} decreases with increasing E_F. As a result, the intraband part of σ'_{xy} concentrates its spectral weight at the lower edge of the plotted spectrum, and displays a much larger amplitude than its interband counterpart, as explained above. Similar conclusions do apply to θ_F as direct inspection of the bottom and top panels do show.

When $N_F = 1$, a significant departure from the semi-classical behavior can be appreciated in the intraband region ($0 - 100$ meV). Remarkably, though, already for $N_F = 2$, the semi-classical Hall conductivity approximates well the quantum result, with a significant deviation only occurring near the interband threshold ($\approx$300 meV), where the semi-classical approach must necessarily fails. These features are in accordance with the general conclusions drawn in Sec. II D.

For comparison, the real part of the longitudinal conductivity is also shown in the bottom panel of Fig. 13. The longitudinal current can be induced by photons which are resonant with any interband transition allowed by the Pauli principle (that is, $\hbar\omega > \hbar\Delta\Omega_{N_F} \simeq 2E_F$) and hence many absorption peaks can be observed. On the contrary, the Faraday rotation essentially depends on σ'_{xy} and therefore is driven only by two resonances.

Dependence on the Fermi energy and magnetic field.— We have seen that when few LLs are occupied, quantum effects come into play and the semi-classical solution no longer gives an accurate description of the Faraday effect. The latter can even happen in the intraband region (see e.g. Fig. 13, mid panel), embodying the departure of the intraband gap Δ_{N_F} from its semi-classical analogous, the cyclotron energy, $\hbar\omega_c$ (see Table I). Given the importance of energy quantization for low electronic density, we expect θ_F to display abrupt behavior when the Fermi energy crosses the first few LLs. The latter behavior should reflect directly the step structure of the optical (or ac-) Hall conductivity $\sigma'_{xy}(\omega)$.[19]

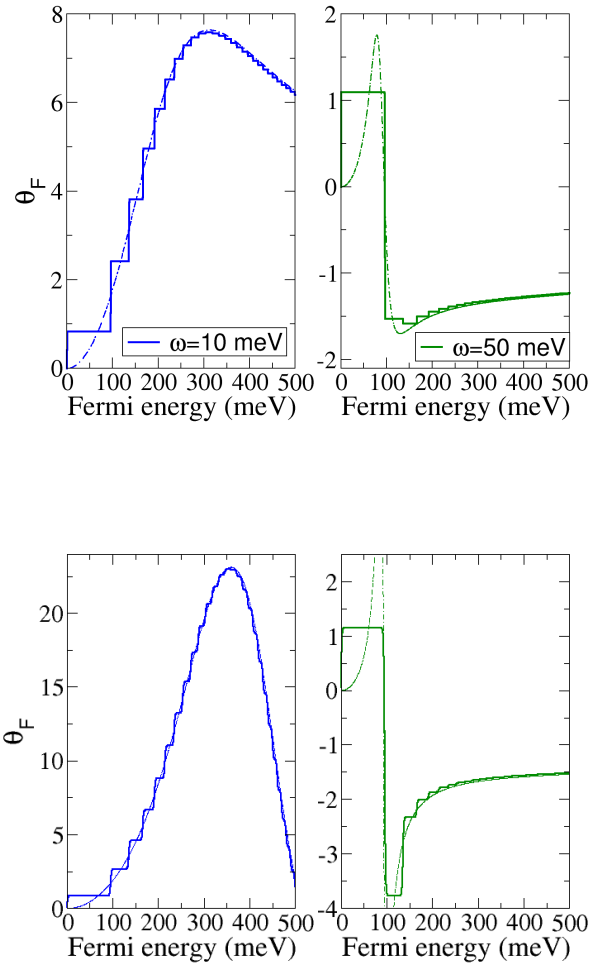

Figure 14: Quantization of the Faraday effect in graphene. **Top**: Faraday rotation angle (given in degrees) for free-standing graphene as function of the Fermi energy at a magnetic field of $B = 7$ T for $\hbar\omega = 10$ meV (left panels) and $\hbar\omega = 50$ meV (right panels). The respective semi-classical result is plotted in the dashed lines. Other parameters: $\Gamma = 10.5$ meV and $T = 12$ K. **Bottom:** The same as the top panel but with $\Gamma = 2$ meV.

Figure 14 shows the Faraday rotation angle against E_F for fixed magnetic field, $B = 7$ T. The heights of the steps are not uniform since the optical Hall conductivity no longer obeys the dc quantization rule [Eq. (64)]. When the Fermi energy crosses higher LLs, the smooth semi-classical result (dashed curves) is recovered.

Combining the approximated formula for θ_F, Eq. (89) [valid for $c\mu\sigma'_{\mp}(\omega) \ll 2$ and $\theta_F \lesssim 1$], and the exact Hall

conductivity at $T = 0$ [Eqs. (57)-(58)], explicit formulae for the steps heights can be obtained. When the Fermi energy crosses LLs with $n > 1$, the expression for $\Delta\theta_F$ becomes somewhat cumbersome. Nevertheless, simple analytical expressions can be obtained in some regimes. For instance, when the small photon energy compared to relevant scales, $\hbar\omega \ll \Gamma \ll E_1$, the steps are predicted to be approximately uniform,

$$\Delta\theta_F^{(n\to n+1)} \simeq \frac{2c\mu e^2}{h} = 4\alpha \simeq 0.03\,\text{rad}, \qquad (93)$$

where α denotes the fine structure constant, $\alpha = e^2/(4\pi\hbar\epsilon_0 c)$. In Ref. [19] for a estimative of the magnitude of the effect it has been assumed that the step height of σ'_{xy} is approximately given by $\Delta\sigma'_{xy}(\omega) \simeq e^2/h$, resulting in $\Delta\theta_F \simeq \alpha$. Rigorously, the step height for the transitions $n = 0 \to n = 1$ is about $4e^2/h$, hence explaining the extra factor of four in our expression. In fact, in the limit $\hbar\omega \ll \Gamma \ll E_1$, the steps in the Hall conductivity will all have approximately the same height, as in the dc case [see Eq. (64)].

In Fig. 14, a decrease of the step's height relative to the estimative value in Eq. (93) can be observed, already for the first step. This happens because the condition $\Gamma \ll E_1$ is too restrictive, and hence we relax this condition to $\Gamma \lesssim E_1$, but at the same time keeping the low photon energy condition, $\hbar\omega \ll \Gamma$. Doing so, leads to a better approximation,

$$\Delta\theta_F^{(n\to n+1)} \simeq \frac{1}{1+(6+4n+\delta_{n,0})\tilde{\gamma}^2}\frac{1}{1+4n\tilde{\gamma}^2} \times 4\alpha\,, \qquad (94)$$

where we have defined the dimensionless parameter $\tilde{\gamma} = \Gamma/E_1$. Using this parameter, the validity condition of Eq. (94) reads, $\tilde{\gamma} \lesssim 1$ and $\hbar\omega \ll \Gamma$.

Two physical scenarios where the Faraday steps are not uniform are shown in Figure 14. In the bottom panel, the transitions $n = 0 \to n = 1$ ($E_F \simeq 100$ meV) come with a variation of θ_F of roughly 1.8° ($\simeq 0.031$ rad) for $\hbar\omega = 10$ meV against $-5.1°$ ($\simeq -0.089$ rad) for $\hbar\omega$ =50 meV, which does not agree with the neither the rough uniform estimative nor with Eq. (94). The reason for this discrepancy is that the condition $\hbar\omega \ll \Gamma$ is not fulfilled for the photon frequencies considered in that figure. Recall that in graphene, Γ is about about 10 meV, and thus infrared photons have $\hbar\omega \gtrsim \Gamma$. It is therefore useful to derive approximate formulae for $\Delta\theta_F$ that is valid in the regime $\hbar\omega \gg \Gamma$. Defining $\tilde{\omega} = E_1/(\hbar\omega)$, we arrive at

$$\Delta\theta_F^{(n\to n+1)} \simeq \frac{4\alpha}{1-2(1+2n)\tilde{\omega}^2+\tilde{\omega}^4}\frac{1-\tilde{\omega}^4}{1-2(3+2n)\tilde{\omega}^2+\tilde{\omega}^4}\,. \qquad (95)$$

Substituting for the respective values of $\tilde{\omega}$, we obtain $\Delta\theta_F^{(0\to 1)} = 1.8°$ and $\Delta\theta_F^{(0\to 1)} = -5.3°$, for $\hbar\omega = 10$ eV and $\hbar\omega = 50$ meV, respectively, which agrees well with the numerical results reported in Fig. 14 for $\Gamma = 2$ meV. As for the steps observed in the top panel of the same figure, they cannot be explained accurately with Eq. (95) since in that case we have $\hbar\omega \approx \mathcal{O}(\Gamma)$. We stress that Eqs. (94)-(95) are only accurate when the statement Eq. (89) provides a good description of the Faraday effect in graphene, which in practice means very high photon energies $\hbar\omega$ (see also Fig. 11). For the parameters used in Fig. 14, where the photon energies are not too high, our analytical expressions for $\Delta\theta_F$ are accurate only for the first few steps.

Figure 15 shows the variation of θ_F with the magnetic field for two cases, i) low doping ($E_F = 0.05$ eV) and ii) high doping ($E_F = 0.3$ eV). In the latter case, we are well inside the semi-classical regime even for the maximum intensity of the magnetic field considered (B =7T), and thus no distinction can be made between the curves computed using the semi-classical conductivity tensor or the EOM formulae. In this regime, the Faraday effect increases monotonously with the magnetic field.

For low electronic density, on the other hand, the agreement between the Boltzmann and EOM formalisms only takes place for low magnetic field. For increasing values of the magnetic fields such agreement ceases to occur as soon as the intraband gap does not match the cyclotron energy $\hbar\omega_c$. Then, energy level quantization becomes important and the EOM expressions must be considered (i.e., N_F is small; see Sec. II E) — this explains the departure from the semi-classical value for θ_F observed in the right panel at $B \approx 1$ T for $\hbar\omega = 10$ meV [$B \approx 0.5$ T for $\hbar\omega = 30$ meV]. If the magnetic field intensity is higher than a given value, we necessarily have $N_F = 0$ (for 0.05 eV this value is about 1.9 T). In such case, the Hall conductivity, at $T = 0$, is fully determined by a single type of interband transition, and, assuming $E_1(B) \gg \hbar\omega, \Gamma$, we obtain [see Eq. (58)],

$$\sigma'_{xy} \underset{\text{large } B}{\simeq} -\frac{2e^2}{h} \Rightarrow \theta_F \simeq 2\alpha \simeq 3\times 10^{-4}\,^\circ\,. \qquad (96)$$

The latter considerations explain the plateau formed at $B \approx 2$ T (blue solid line) in the right-panel of Fig. 15. The red dashed double dotted line corresponds to photons with higher energy, shifting the formation of the plateau towards higher fields. Eq. (96) is indeed the high magnetic field limit [$E_1(B) \gg$ energy scales] of the Faraday rotation induced by single-layer graphene.

Although the measured Faraday rotation angle is remarkably large given that it comes from a single graphene layer, in both low and high doping regimes (see Fig. 15), so it is the needed magnetic field, $B \gtrsim 1$ T. The goal in then to obtain large Faraday rotation angles using graphene and modest fields at the same time. A simple idea that uses the non-reciprocity of the Faraday effect is to enclose graphene in between two mirrors. We discuss this possibility in the following section.

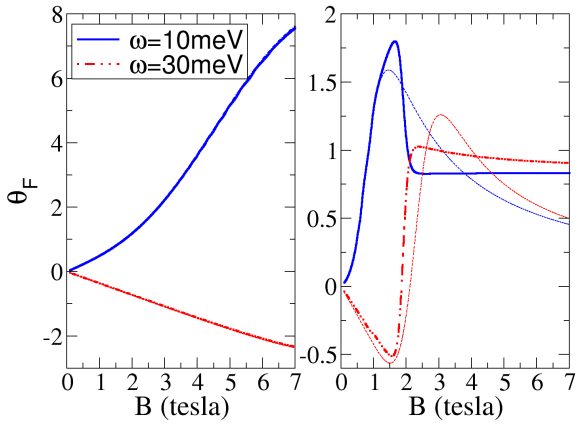

Figure 15: Faraday rotation angle (given in degrees) as function of the magnetic field for $E_F = 0.30$ eV (left panel) and $E_F = 0.05$ eV (right panel). In each panel two photon energies are represented: $\hbar\omega = 10$ meV (blue solid line) and for $\hbar\omega = 30$ meV (red dashed double dotted line) with respective semi-classical counterparts in dashed lines. Other parameters as in top panel of Fig. 14.

D. Enhancement of Faraday rotation in a cavity geometry

We have seen that the existence of intraband and interband transitions in graphene permit to generate finite (non-zero) Faraday rotations in different ranges of the electromagnetic spectrum. In doped graphene ($N_F \geq 1$), for instance, the intraband gap is bounded from above by

$$E^{\rm intra} \leq \Delta_1 = E_2 - E_1 \simeq 15\sqrt{B}\,{\rm meV}\cdot{\rm T}^{-1/2}\,, \qquad (97)$$

implying that, by using magnetic field intensities $\sim 1\,$T, graphene can be exploited for magneto-optical applications from the microwave up to the far-infrared regimes $f = E/h \lesssim 3.6$ THz (an example of THz Faraday rotation driven by intraband transitions can be found in Fig. 12). Another possibility is to make use of transitions connecting the valence and conduction Dirac cones, whose interband gaps are bounded from below,

$$E^{\rm inter} \geq \hbar\Delta\Omega_1 = E_1 \simeq 36\sqrt{B}\,{\rm meV}\cdot{\rm T}^{-1/2}\,, \qquad (98)$$

thus accomplishing for far-infrared up to visible light light frequencies (an example of mid-infrared Faraday rotation driven by interband transitions is shown in Fig. 13). We recall that increasing the electronic density in order to obtain even larger interband gaps ($\hbar\Delta\Omega_n$ with $n > 1$), and thus shifting the magneto-optical response of graphene above the mid-infrared, $\hbar\omega \sim \hbar\Delta\Omega_{N_F} \simeq 2E_F$, originates optical Hall conductivity peaks with low intensity. As a consequence, very small Faraday rotations are produced already in the near-infrared regime. A good estimate for the maximum achievable interband-induced Faraday rotation can be obtained from Eqs. (63) and (89),

$$\max|\theta_F| \simeq \left(\frac{eBv_F^2}{2\omega\Gamma}\right)\times\alpha\,, \qquad (99)$$

which, for example, taking $B = 7$ T , $\Gamma = 10$ meV and $\hbar\omega = 1$ eV leads to $\max|\theta_F| \simeq 10^{-3}$. Although the amount of THz Faraday rotation, $\hbar\omega \simeq O({\rm meV})$, reported in our figures are well within state-of-art capabilities [the resolution for Faraday measurements in THz time-domain spectroscopy is presently limited to one mrad[20] (∼0.06 degrees)], high magnetic fields ~ 1 T are still needed which can be a disadvantage for specific applications; moreover, according to Eq. (99) the needed magnetic field increases as higher photon frequencies are to be probed.

The situation is very different in other two-dimensional electron gases, for which θ_F is proportional to the sample's thickness (as the light travels farther through the material, more Faraday rotation accumulates). Single-layer graphene, on the other hand, being one-atom thick an hence truly two-dimensional, requires the use of high magnetic fields in order to detect Faraday rotations. It is therefore natural to ask whether it is possible to conceive a setup leading to accumulation of Faraday effect; ideally, such setup would avoid the use of several samples and, at the same time, take advantage of the broad magneto-optical response of single-layer graphene.

In what follows, we discuss a graphene-based system that can enhance the intrinsic graphene's Faraday rotation at any frequency and thus can cope with the difficulty above-mentioned. The idea consists in enclosing graphene into an optical cavity: due to intra-cavity interference, photons undergo several round trips within the cavity before leaking out. Loosely speaking, due to non-reciprocity of the Faraday effect, accumulation of θ_F then takes place each time a photon passes through graphene — a sketch of the experimental apparatus is shown in Fig. 16.

Explicit calculations (see below) show that giant Faraday rotations are achieved even when the optical *finesse* of the cavity is modest. The optical *finesse* can be easily tuned by changing the reflectivity of the end-mirrors: the higher the latter quantity, the larger is the number of round trips of photons inside the cavity and hence further Faraday accumulation occurs. Indeed, the cavity geometry gives a straightforward solution to mimic the effect of a sample's thickness (absent in single-layer graphene).

Following the steps of Sec. III A, we write the boundary conditions of the electromagnetic field in terms of circularly polarized waves. Employing similar notation, we define the input and output circular vector amplitudes,

$$\boldsymbol{\mathcal{E}}_{\pm}^{\rm in} = \left(E_{\pm}^{\rm in}\,, E_{\pm}^{\rm r}\right)^T\,, \qquad (100)$$

$$\boldsymbol{\mathcal{E}}_{\pm}^{\rm out} = \left(E_{\pm}^{\rm t}\,, 0\right)^T\,, \qquad (101)$$

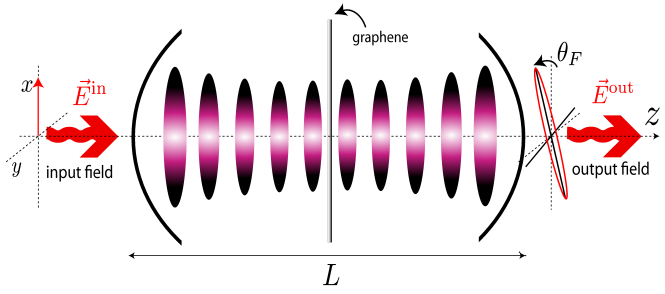

Figure 16: Schematic of the graphene-optical cavity system: linearly polarized light shines into an optical cavity with graphene placed at the center. The field inside the cavity perceives graphene as an extra boundary and hence the two halves of the cavity operate as independent cavities of effective size $L/2$. Matching the light frequency $\hbar\omega$ with a resonant frequency of the cavity $\omega = n\pi c/L$ ($n \in \mathbb{N}$) traps photons inside the cavity for several round trips. As a consequence, Faraday rotation accumulates due to multiple passages through graphene leading to an output field with a large Faraday rotation.

respectively (see also Fig. 16), where $E^{\rm in}_{\pm} = E^{\rm in}_x \pm iE^{\rm in}_y$ (the reflected $E^{\rm r}_{\pm}$ and transmitted waves $E^{\rm t}_{\pm}$ having analogous definitions). The first (second) component of the vectors Eq. (100)-(101) refers to the complex amplitude of light traveling in the positive (negative) z direction.

The output field, $\boldsymbol{\mathcal{E}}^{\rm out}_{\pm}$, and thus the total Faraday rotation angle, can be more conveniently computed using the transfer matrix formalism. The method is explained in detail in Appendix A. Here, we just state the basic results: the $T-$matrix, by definition, connects the input and output vector amplitudes, according to

$$\boldsymbol{\mathcal{E}}^{\rm in}_{\pm} = T^{\rm in\to out}_{\pm}\boldsymbol{\mathcal{E}}^{\rm out}_{\pm}\,, \tag{102}$$

where $T^{\rm in\to out}_{\pm}$ is a product of individual t-matrices for each boundary (optical component, metallic surface, etc.). Its inverse permits to compute $\boldsymbol{\mathcal{E}}^{\rm out}_{\pm}$ given the input field $\boldsymbol{\mathcal{E}}^{\rm in}_{\pm}$, and hence the optical characteristics of the cavity-graphene system. In particular, the circular transmitted amplitudes, $t_{\pm} = E^{\rm t}_{\pm}/E^{\rm in}_{\pm}$, are given by $t_{\pm} = 1/[T^{\rm in\to out}_{\pm}]_{1,1}$.

For the geometry posed in Fig. 16, the input-output $T-$matrix reads

$$T^{\rm in\to out}_{\pm} = T_{\rm m}\cdot\begin{bmatrix} e^{-i\omega L/2c} & 0 \\ 0 & e^{i\omega L/2c}\end{bmatrix}\cdot T^{\rm g}_{\pm} \cdot\begin{bmatrix} e^{-i\omega L/2c} & 0 \\ 0 & e^{i\omega L/2c}\end{bmatrix}\cdot T_{\rm m}\,. \tag{103}$$

Each operator in Eq. (103) propagates the electric field to the right until a boundary is reached. $T_{\rm m}$ encodes the effect of the first interface, a mirror, and depends only on the mirror's transmission and reflection amplitudes, t and r, respectively. It can be written as

$$T_{\rm m} = \frac{1}{i|t|}\begin{bmatrix} 1 & |r| \\ -|r| & -1\end{bmatrix}\,. \tag{104}$$

(For a derivation, see e.g. Ref. 52.) After interaction with the left-end mirror, photons can enter into the cavity and propagate for a distance of $L/2$ before the next interaction. This means that another $T-$matrix is needed; free propagation merely adds a phase to the electric field [see Eq. (A5) and text therein] and thus is represented by a di-

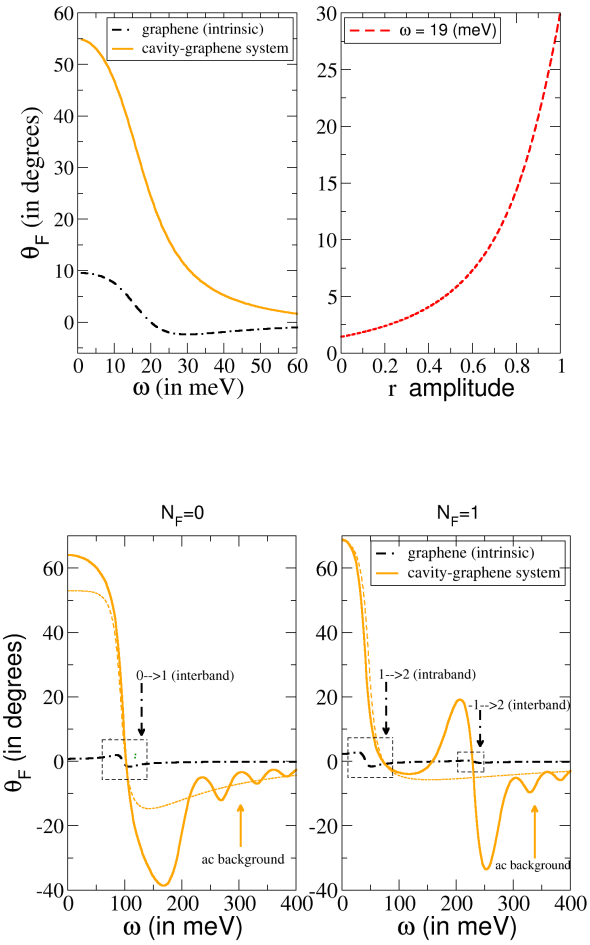

Figure 17: Faraday rotation angle of a cavity-graphene system in the semi-classical and quantum regimes. **Top panels:** Left—θ_F as function of the photon energy for a cavity-graphene system in a magnetic field of 7 T . The Fermi energy reads $E_F = 0.3$ eV and the cavity mirrors have $r = 0.99$. Other parameters: $\Gamma = 10.5$ meV and $T = 12$ K. Right—θ_F versus the reflection amplitude r for $\hbar\omega = 19$ meV. **Bottom panels:** In the left (right) panel, the Fermi energy reads $E_F = 0.05$ eV ($E_F = 0.1$ eV) which corresponds to a Landau level occupation of $N_F = 0$ ($N_F = 1$). The orange dashed line shows θ_F as obtained with the semi-classical conductivity tensor.

agonal matrix, which is the second operator in Eq. (103). At $z = L/2$, photons arrive at the air-graphene-air interface, whose $T-$matrix we denote by $T^{\rm g}_{\pm}$. (More involved types of interfaces could be considered: for example, air-substrate-graphene-air. The present choice has the advantage of keeping the mathematical expressions elegant; generalization to other configurations using the present formalism is straightforward.) The graphene's $T-$matrix depends on the magnetic field intensity, electronic density, temperature, and LL broadening, via the complex optical conductivity of graphene $\sigma_{\pm}(\omega)$; its explicit form is

$$T^{\rm g}_{\pm} = \frac{1}{2}\begin{bmatrix} 2+Z_0\sigma_{\mp}(\omega) & Z_0\sigma_{\mp}(\omega) \\ -Z_0\sigma_{\mp}(\omega) & 2-Z_0\sigma_{\mp}(\omega) \end{bmatrix}, \qquad (105)$$

where $Z_0 = \mu_0 c$ denotes the vacuum impedance—see Appendix A for a detailed derivation. Finally, the second line of Eq. (103) propagates the field in free space for a distance of $L/2$ and adds the right-end mirror.

The Faraday rotation angle is obtained from $\theta_F = (1/2)\arg(t_+/t_-)$, with the circular amplitudes ratio t_+/t_- given by $[T^{\rm in\to out}_-]_{1,1}/[T^{\rm in\to out}_+]_{1,1}$ [Eq. (A7)]. After some algebra, we arrive at

$$\frac{t_+}{t_-} = \frac{2+Z_0\sigma_+(\omega)-|r|\,[Z_0\sigma_+(\omega)-2]\,e^{i\omega L/c}}{2+Z_0\sigma_-(\omega)-|r|\,[Z_0\sigma_-(\omega)-2]\,e^{i\omega L/c}}, \qquad (106)$$

from which θ_F can be immediately deduced. Setting $r = 0$ in the latter expression leads to the previous result in the absence of a cavity [compare with $t_\pm$ as obtained from Eq. (83) with $\epsilon_r = 1$].

When $r > 0$, interference takes place and photons can make several round trips before being transmitted through the cavity. On a intuitive basis, we then expect that the Faraday rotation angle can be enhanced due to multiple passages of photons through graphene, which indeed is the case as shown in Fig. 17. Hereafter, the size of the cavity is set to $L = n\pi c/\omega$, with n odd. The solid line shows θ_F for the cavity-graphene system and the dashed-dot line shows θ_F for free-standing graphene for the same parameters: clearly, in the range of frequencies considered, the Faraday effect is greatly enhanced. For example, for low frequency $\hbar\omega \approx 10$ meV, θ_F has increased by a factor of about 5, reaching a value of 55 degrees, whereas for $\hbar\omega \approx 19$ meV, θ_F increases by a factor of about 20, reaching a value of approximately 25 degrees.

Direct inspection of Eq. (106) discloses the observed boost of Faraday effect: when $r \to 1$ and the phase factor $\exp(i\omega L/c) = -1$, the constant factor of 2 in the both the denominator and numerator cancels, leading to,

$$\left|\frac{t_+}{t_-}\right| e^{2i\theta_F} \underset{\substack{n\,\text{odd}\\ r\simeq 1}}{\simeq} \frac{\sigma_+(\omega)}{\sigma_-(\omega)}, \qquad (107)$$

which can present large arguments, $2\theta_F$. The opposite limit, $r \to 0$, in which the isolated graphene system is recovered, leads to much smaller arguments, since generally $2 \gg Z_0 {\rm Im}\,\sigma_\pm$, which implies that the real part of Eq. (83) is predominant. Choosing a cavity mode with n odd and $r \simeq 1$ is fully equivalent to take a large number of equally prepared graphene sheets placed in a row (Appendix B). The cavity geometry therefore permits to take advantage of large Faraday rotation accumulation using a single graphene sheet.

In a cavity geometry, the Faraday rotation is no longer dominated by the behavior of $\sigma'_{xy}(\omega)$ [see Eq. (89)], for θ_F now depends on the full conductivity tensor [Eq. (107)]. The most visible consequence of the latter fact is that photons with $\hbar\omega \approx 20$ meV undergo considerable Faraday rotation angles in a cavity geometry, whereas, in a single passage through graphene, photons with such energy do not produce Faraday rotation at all (Fig. 17). This apparently counter-intuitive result is due to induced ellipticity in single passages and is explained in Appendix B.

Semi-classical versus quantum regimes in a cavity geometry—Fig. 17 (top panel) considers the case of $E_F = 0.3$ eV and $B = 7$ T, well inside the semi-classical regime, for which the ac conductivity is dominated by intraband contributions in a wide range of frequencies (Sec. II); the corresponding intraband Faraday rotation is seen to be greatly enhanced in the cavity geometry.

The low electronic density regime of the cavity-graphene system is shown in the bottom panel of Fig. 17. Remarkably, for energies above the interband threshold, namely, $\hbar\omega \gtrsim E_1 \simeq 95$ meV for $N_F = 0$ (left panel) and $\hbar\omega \gtrsim E_1 + E_2 \simeq 230$ meV for $N_F = 1$ (right panel), $\theta_F(\omega)$ presents a qualitative different behavior from an isolated graphene sheet (black dot double-dashed curve): oscillations do emerge. These oscillations are hindered in single photon passages through graphene (see also Fig. 13), but for multiple photon passages, in the high frequency limit, Shubnikov–de Haas oscillations in the longitudinal conductivity $\sigma_{xx}(\omega)$ (Fig. 4) are critical in defining the orientation of the light polarization axes. These oscillations are obviously absent in the semi-classical Boltzmann calculation (orange dashed curve). In the top panel, where $E_F = 0.3$ eV, such oscillations are not present because the represented photon energies are well below the threshold for interband transitions $\hbar\omega \simeq 2E_F$.

Near infrared and visible range Faraday rotation— We finish this section by mention an important application of the cavity-graphene system: interband-induced Faraday rotations in the near-infrared and visible regimes. Figure 18 shows that energetic photons can attain $\theta_F \gtrsim 1$ by tuning the Fermi energy to sufficiently high values. In this regard, the top panel shows numerical data for graphene with $E_F = 0.85$ eV; such high doping level of graphene samples are feasible using chemically synthesized graphene with ferroelectric substrates (instead of the conventional SiO_2).[53]

Given the mirrors reflection amplitude considered, $r = 0.99$, photons are trapped for a large number of round trips. This means that is highly probable that photons get absorbed by graphene before leaking the cavity. This

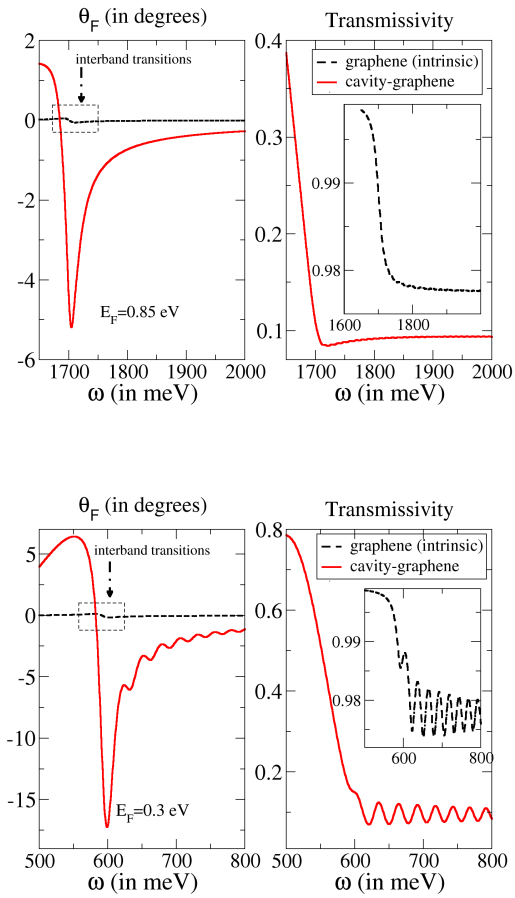

Figure 18: Faraday rotation boost in the infrared and visible ranges. **Left panels**: Faraday rotation angle versus photon energy of a cavity-graphene system with $E_F = 0.85$ eV (top) [$E_F = 0.3$ eV (bottom)]. **Right panels**: The transmissivity of the cavity-graphene system for the same parameters considered in the left panels (Inset: transmissivity of intrinsic graphene for the same parameters). Other parameters as in Fig. 17. In order to obtain a measurable Faraday rotation at $\hbar\omega \approx 1.7$ eV (red light) [$\hbar\omega \approx 0.5$ eV (infrared)] it is necessary to tune the intraband resonance according to $E_F \simeq \hbar\omega/2$.

explains why the transmissivity of the cavity-graphene system, as shown in the right panel of Fig. 18, is well below one (but still large enough that the effect can be measured). One way of increasing the transmissivity of the cavity-graphene system is to decrease the quality of the mirrors at the expense of decreasing the maximum achievable θ_F.

We finally remark that, non-linearity associated with next-neighbor hopping t' in the honeycomb graphene lattice can play a role for photons with $\hbar\omega \gtrsim 1$ eV, and hence corrections to the Dirac cone approximation (Sec. II A) and thus to the EOM solutions may exist; such corrections are however expected to be very small.[14]

IV. CONCLUSION AND OUTLOOK

In the first part of this work, the EOM method has been adapted to the study of magneto-optical transport of electronic systems. To illustrate the method, the magneto-optical conductivity tensor of single-layer graphene in the Dirac cone approximation has been derived, accounting for both intraband (semi-classical) transitions and interband transitions between the valence and conduction bands.

The general regularization procedure to obtain the regular conductivity tensor from the solutions of the EOM for the current operator has been established; such procedure is shown to lead to the correct formulae without the need for evaluating the Kubo formula. To the best of the authors knowledge such procedure has not been discussed so far in the literature. In addition, quantitative comparisons between the quantum EOM solutions and the semi-classical Boltzmann formulae, in the full optical spectrum, and both in low and high doped graphene samples, have been given throughout.

In a second part, the Faraday rotation effect in single-layer graphene has been studied in detail; in particular, simple formulae for the steps' heights in the quantum Hall regime have been derived. Our results have been shown to account well for available experimental data in the semi-classical regime.

Last, we have proposed a simple experimental apparatus based on a optical cavity that permits to enhance the Faraday rotation of graphene by orders of magnitude, thus allowing to obtain giant Faraday rotation angles in the infrared region and modest Faraday rotation angles in the visible region.

We hope that the present work further stimulates the research of magneto-optical properties of ultra-thin two-dimensional gases and graphene-based solid state devices.

Acknowledgments

A.F. acknowledges FCT Grant No. SFRH/BPD/65600/2009. N.M.R.P. acknowledges Fundos FEDER, through the Programa Operacional Factores de Competitividade - COMPETE and by FCT under project no. Past-C/FIS/UI0607/2011. A.H.C.N. acknowledges support from the DOE grant DE-FG02-08ER46512 and the ONR grant MURI N00014-09-1-1063.

Appendix A: Transfer matrix formalism

The transfer matrix ($T-matrix$) approach is a widely-used method in optics and related fields and provides an efficient mean of calculating the amplitude and phase of transmitted electric fields through and arbitrary number of interfaces. In this appendix, we give a self-contained

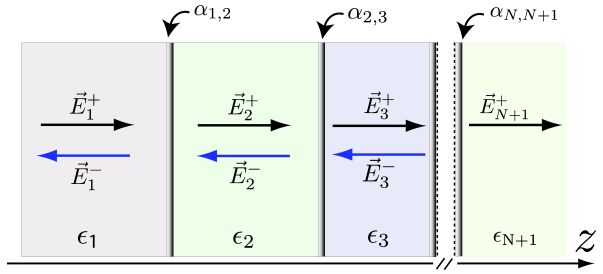

Figure 19: Schematic of an optical system consisting of an array of interfaces separated by different types of dielectric media. An electromagnetic wave, $\boldsymbol{E}^{\rm in} = \boldsymbol{E}_1^+$, coming from a medium with dielectric permittivity ϵ_1 interacts with an interface α_{12}. As a result, it is partially reflected and partially transmitted into the medium ϵ_2. Equivalent events take place at the remaining interfaces. The vectors with superscript $+(-)$ denote the component of the electric field traveling in the positive (negative) direction of z. An uniform static magnetic field $\mathbf{B} = B\mathbf{e_y}$ is assumed.

review of the method and derive explicitly the $T-$matrix for a general two-dimensional conducting media.

1. General formalism

For concreteness, we assume that an incident electromagnetic wave of frequency ω, travels in the z direction through a set of N metallic interfaces, placed normal to the direction of propagation, with labels $\alpha_{n,n+1}$, and located at positions $z = z_n$ $(n \in 1, 2, ...N)$. These interfaces are separated by dielectric mediums — Fig. 19 shows the configuration we have in mind.

The electric field is separated according to the direction of propagation: $\boldsymbol{E}_n^+(z)$ represents the part the electric field traveling in the positive direction of z, within the region n, whereas $\boldsymbol{E}_n^-(z)$ represents the part traveling in the opposite direction.

As shown below, the calculation of transmitted and reflected amplitudes becomes easier by writing the boundary conditions in terms of circularly polarized waves (see also Sec. III A). Therefore, we focus on the circular amplitudes,

$$E_{n,\tau}^{\pm}(z) = E_{n,x}^{\pm}(z) + i\tau E_{n,y}^{\pm}\,, \tag{A1}$$

where τ is the polarization index: $\tau = \pm 1$ [$+1(-1)$ means right-handed (left-handed) circular polarization]. Indeed, in a given region i, the total (complex) electric field is the sum of both components,

$$\boldsymbol{E}_n(z,t) = \boldsymbol{E}_n^+(z)e^{-i\omega t} + \boldsymbol{E}_n^-(z)e^{-i\omega t}\,. \tag{A2}$$

The physical electric field is obtained by taking the real part of the latter expression. We omit the time-dependence in the remainder of the appendix.

The $T-$matrix connects the amplitude of the electric field to the left and to the right of a given boundary (interface). Take for instance, the interface labeled $\alpha_{1,2}$ in Fig. 19. The respective $T-$matrix, $\hat{T}^{1,2}$, is defined as,

$$\begin{pmatrix} E_{2,\tau}^+(z_1^+) \\ E_{2,\tau}^-(z_1^+) \end{pmatrix} = \hat{T}_\tau^{1,2} \begin{pmatrix} E_{1,\tau}^+(z_1^-) \\ E_{1,\tau}^-(z_1^-) \end{pmatrix}\,, \tag{A3}$$

where $z_1^{\pm}$ denote the position where the electric field is to be evaluated: right after $(+)$ or before $(-)$ the interface located at $z = z_1$. For ease of notation, we define the vector of amplitudes,

$$\mathcal{E}_{n,\tau}(z) = \begin{pmatrix} E_{n,\tau}^+(z) \\ E_{n,\tau}^-(z) \end{pmatrix}\,, \tag{A4}$$

and drop the superscripts in the coordinates z_n.

If more than one interface is present, the light propagates a given distance before interacting with the next component. Propagation of light through a dielectric medium merely adds a phase to each τ circular component of the electric field. Indeed, its action can be represented by a diagonal matrix,

$$\mathcal{E}_{n,\tau}(z_i) = \begin{bmatrix} e^{-ik_n\Delta z_n} & 0 \\ 0 & e^{ik_n\Delta z_n} \end{bmatrix} \mathcal{E}_{n,\tau}(z_{i+1})\,, \tag{A5}$$

where the index n just takes the values for which there is intermediate light propagation, i.e., $n = 1, ..., N-1$, the wave vector depends on the dielectric medium according to $k_n = \omega\sqrt{\epsilon_n}/c$ and $\Delta z_n = z_{n+1} - z_n$ is the width of the region n. Note that Eq. (A5) defines a particular case of a $T-$matrix, which we denote by $\hat{F}_n$.

The problem of finding how the output electric field, of definite polarization τ, immediately after leaving the last interface, $E_{N+1,\tau}^+(z_N)$, relates to the incoming electric field, with the same polarization τ, $E_{1,\tau}^+(z_1)$, then amounts to take the product of the individual t-matrices,

$$\mathcal{E}_{1,\tau}(z_1) = \underbrace{\hat{T}_\tau^{1,2}\hat{F}_2\hat{T}_\tau^{2,3}...\hat{T}_\tau^{N-1,N}\hat{F}_N\hat{T}_\tau^{N,N+1}}_{\hat{T}_\tau^{\rm in\to out}}\mathcal{E}_{N+1,\tau}(z_N)\,. \tag{A6}$$

The total $T-$matrix $\hat{T}_\tau^{\rm in\to out}$ has the desired information,

$$\frac{E_{N+1,\tau}^+}{E_{1,\tau}^+} = 1/\left[\hat{T}_\tau^{\rm in\to out}\right]_{1,1}\,. \tag{A7}$$

As for the relation between the output field and the reflect field at the first boundary, $E_{1,\tau}^-(z_1)$, we obtain,

$$\frac{E_{N+1,\tau}^+}{E_{1,\tau}^-} = 1/\left[\hat{T}^{\rm in\to out}\right]_{2,1}\,. \tag{A8}$$

In what follows, we show how to construct the $T-$matrix for a general two-dimensional conducting medium. Knowledge of the t-matrices allows to determine the characteristics of transmitted and reflected light through a general set of conducting two-dimensional thin films, mirrors, etc., by employing Eq. (A6).

2. T-matrix for a general conducting 2D interface

We restrict the present derivation to non-magnetic media, and assume the standard constitutive relations do hold,

$$\boldsymbol{D}(\mathbf{r},\omega) = \epsilon(\mathbf{r},\omega)\boldsymbol{E}(\mathbf{r},\omega)\,, \tag{A9}$$
$$\boldsymbol{J}(\mathbf{r},\omega) = \hat{\sigma}(\mathbf{r},\omega)\boldsymbol{E}(\mathbf{r},\omega)\,, \tag{A10}$$

where $\boldsymbol{D}$, ϵ, and σ denote the displacement field, permittivity and conductivity, respectively. Also, and without prejudice, we take the two-dimensional conducting interface to be located at $z = 0$. The $T-$matrix is defined as

$$\begin{pmatrix} E^+_{a,\tau}(z=0^-) \\ E^-_{a,\tau}(z=0^-) \end{pmatrix} = \hat{T}^{(ab)}_\tau \begin{pmatrix} E^+_{b,\tau}(z=0^+) \\ E^-_{b,\tau}(z=0^+) \end{pmatrix}, \tag{A11}$$

where a (b) is the keep-booking index for the medium at the left (right) of the interface.

Various constraints emerge due to continuity of $\boldsymbol{E}$ (and its derivative) at the 2D conducting interface. Indeed, Maxwell equations imply,

$$\boldsymbol{E}_a(0) = \boldsymbol{E}_b(0)\,, \tag{A12}$$
$$\left(\frac{\partial \boldsymbol{E}_a}{\partial z}\right)_{z=0} - \left(\frac{\partial \boldsymbol{E}_b}{\partial z}\right)_{z=0} = i\omega\mu_0\hat{\sigma}\boldsymbol{E}_b(0)\,, \tag{A13}$$

where the conductivity tensor reads

$$\hat{\sigma} = \sigma_{ij}(\omega)\delta(z)\,. \tag{A14}$$

The conductivity depends on the light frequency ω, and generally also on other quantities (Fermi energy of the interface, temperature, etc.). In the latter expression, the subscripts $i, j = x, y$ are Cartesian coordinates. In terms of circularly polarized fields, Eq. (A13) reads,

$$k_a(E^+_{a,\tau} - E^-_{a,\tau}) - k_b(E^+_{b,\tau} - E^-_{b,\tau}) = \omega\mu_0 \times \\ \times (E^+_{b,\tau} + E^-_{b,\tau})\sigma_{-\tau}(\omega)\,, \tag{A15}$$

where we have admitted an isotropic medium, $\sigma_{xx} = \sigma_{yy}$, and have defined

$$\sigma_\pm(\omega) = \sigma_{xx}(\omega) \pm i\sigma_{xy}(\omega)\,. \tag{A16}$$

The statement Eq. (A15) shows that the two circularly polarizations are decoupled, even in the presence of a complex conductivity $\sigma_\pm(\omega)$. This is the reason why it is advantageous to write the boundary conditions in terms of circularly polarize fields (Sec. III A).

According to the definition of $T-$matrix [Eq. (A11)], we need to relate $E^+_{a,\tau}$ with $E^\pm_{b,\tau}$ and $E^-_{a,\tau}$ with $E^\pm_{b,\tau}$, separately. To do so, we make use of the continuity condition Eq. (A12) written in circular waves, $E^+_{a,\tau} + E^-_{a,\tau} = E^+_{b,\tau} + E^-_{b,\tau}$, in order to arrive at,

$$\pm 2k_a E^\pm_{a,\tau} = k_b(E^+_{b,\tau} - E^-_{b,\tau}) \\ + [\omega\mu_0\sigma_{-\tau}(\omega) \pm k_a](E^+_{b,\tau} + E^-_{b,\tau})\,. \tag{A17}$$

Combining Eq. (A11) and the latter expression, we arrive at the desired result,

$$\hat{T}^{(ab)}_\tau = \frac{1}{2k_a}\begin{bmatrix} \Lambda^{ab}_{\tau,++} & \Lambda^{ab}_{\tau,-+} \\ \Lambda^{ab}_{\tau,--} & \Lambda^{ab}_{\tau,+-} \end{bmatrix}, \tag{A18}$$

where

$$\Lambda^{ab}_{\tau,\pm\pm} = k_a \pm k_b \pm \omega\mu_0\sigma_{-\tau}(\omega)\,. \tag{A19}$$

3. Example: T-matrix of suspended graphene

The $T-$matrix of suspended graphene can be obtained immediately from Eq. (A16). Admitting that the mediums at left and right of the single-layer graphene sheet are air, we obtain,

$$\hat{T}^{\rm graph}_\tau = \frac{1}{2}\begin{bmatrix} 2 + Z_0\sigma^{\rm graph}_{-\tau}(\omega) & Z_0\sigma^{\rm graph}_{-\tau}(\omega) \\ -Z_0\sigma^{\rm graph}_{-\tau}(\omega) & 2 - Z_0\sigma^{\rm graph}_{-\tau}(\omega) \end{bmatrix}, \tag{A20}$$

where $Z_0 = \mu_0 c$ is the vacuum impedance.

Appendix B: Faraday Effect

In the present section, we derive the exact analytical conditions for existence of Faraday rotation and discuss their modification when graphene is enclosed in an optical cavity. Despite the focus on graphene, most of the conclusions drawn here apply generally for systems possessing in-plane symmetry. Once again, for simplicity, we consider the case of suspended graphene; generalization to the case of graphene on top of a substrate is straightforward using the general formulae given in Appendix A.

1. Conditions for Faraday effect in free space

We consider a target graphene sheet, placed on the xy plane, subjected to a normally incident electromagnetic wave, linearly polarized along the x axis, $E_x e^{-i\omega t}$. The magneto-optical Faraday effect takes place when a magnetic field $\boldsymbol{B} = Be_z$ is applied. Then, Lorentz force acts on free carriers producing a Hall electronic ac-current, which in specific conditions (see below), will produce out-of-phase radiation polarized transversely to the impinging field, $E_y e^{-i\omega t}e^{i\phi}$. As a consequence, the resulting electromagnetic wave sees its polarization plane rotated.

Without loss of generality, consider the graphene sheet to be placed at $z = 0$. In the circular basis, $\boldsymbol{e}_\tau = (1/2)(\boldsymbol{e}_x + \tau i\boldsymbol{e}_y)$, the electromagnetic field at $z = 0^-$, reads,

$$\boldsymbol{E}(0^-) = E_0 e^{-i\omega t}(\boldsymbol{e}_+ + \boldsymbol{e}_-)\,. \tag{B1}$$

Note that the actual electric field is given by the real part of the latter equation. After interaction with

graphene, each of the circular components $\tau = \pm 1$ change according to Eq. (A20). The field right after the graphene plane is given by

$$\boldsymbol{E}(0^+) = E_0 e^{-i\omega t}\left[\frac{1}{1+\beta_-}\boldsymbol{e}_+ + \frac{1}{1+\beta_+}\boldsymbol{e}_-\right], \quad \text{(B2)}$$

with $\beta_\pm = Z_0\sigma_\pm(\omega)/2$. To determine whether the plane of polarization has rotated, we write the latter equation in the Cartesian basis,

$$\boldsymbol{E}(0^+) = \frac{E_0 e^{-i\omega t}}{2(1+\beta_+)(1+\beta_-)}\times \\ \times\left[(2+Z_0\sigma_{xx})\,\boldsymbol{e}_x - Z_0\sigma_{xy}\boldsymbol{e}_y\right], \quad \text{(B3)}$$

where we have used the definition of $\beta_\pm$ to simplify the term inside brackets. Obviously, no Faraday rotation takes place when $\sigma_{xy}(\omega) = 0$. On the other hand, having $\sigma_{xy}(\omega) \neq 0$ does not suffice to rotate the polarization plane; linear polarization can change to elliptic polarization with main axes along x and y (this is the case for $B = 5$ T and $\hbar\omega \approx 15$ meV, as shown in the top panel of Fig. 11: elliptic polarized light leaves the graphene sheet, $\delta \approx 0.15$, but still $\theta_F = 0$). For this reason, the actual condition for existence of Faraday rotation is

$$|\sigma_{xy}| > 0 \wedge \mathrm{Arg}\left(\frac{2+Z_0\sigma_{xx}}{Z_0\sigma_{xy}}\right) \neq \pm(2m+1)\frac{\pi}{2}, m \in \mathbb{N}_0\,. \quad \text{(B4)}$$

The amount of Faraday rotation is given by Eq. (85) and thus can be obtained directly from Eq. (B2), reading,

$$\theta_F = \frac{1}{2}\mathrm{Arg}\left(\frac{2+Z_0\sigma_-}{2+Z_0\sigma_+}\right). \quad \text{(B5)}$$

In many situations (e.g. high photon energies and high electronic density), the longitudinal conductivity obeys $Z_0\sigma''_{xx} \ll 2 + Z_0\sigma'_{xx}$, thus leading to the approximate condition, $|\sigma'_{xy}| > 0 \Rightarrow \theta_F > 0$. This is consistent with the approximated formula derived for the Faraday rotation angle [Eq. (89)] which states that θ_F is proportional to σ'_{xy} (see also Fig. 11).

2. Conditions for Faraday effect in an optical cavity

In Sec. III D, we have seen that large Faraday rotations θ_F can be achieved in the cavity-graphene system, even for such photon energies that do not originate Faraday rotation in free space. An example is given in Fig. 17: in free space, impinging light with $\hbar\omega \approx 20$ meV does not change its polarization direction, $\theta_F = 0$, whereas θ_F can be as large as 25^{o} for graphene mounted on a cavity geometry.

In order to explain the above-described phenomenon, it is sufficient to consider the simplified situation where a normally incident photon interacts with graphene twice in a row. For concreteness, we take two graphene samples, equally prepared, separated by a given distance W. Let the photon frequency $\bar{\omega}$ be such that no Faraday rotation is produced in the passage through the first graphene sample, that is,

$$\mathrm{Arg}\left[\frac{2+Z_0\sigma_{xx}(\bar{\omega})}{Z_0\sigma_{xy}(\bar{\omega})}\right] = \pm(2m+1)\frac{\pi}{2}, \quad \text{(B6)}$$

for some $m \in \mathbb{N}_0$ [see Eq. (B4)]. In the latter expression, it is assumed that $\sigma_{xy}(\bar{\omega}) \neq 0$ which is the case when a magnetic field is present. In these conditions, after the first passage, the electric field [Eq. (B3)], can be written as

$$\boldsymbol{E}_1 = \frac{E_0 e^{-i\bar{\omega}t}}{2[1+\beta_+(\bar{\omega})][1+\beta_-(\bar{\omega})]}e^{i\phi}\times \\ \times\left[|2+Z_0\sigma_{xx}(\bar{\omega})|\,\boldsymbol{e}_x \pm i\,|Z_0\sigma_{xy}(\bar{\omega})|\,\boldsymbol{e}_y\right], \quad \text{(B7)}$$

where $\phi = \mathrm{Arg}[2+Z_0\sigma_{xx}(\bar{\omega})]$ and the sign $\pm$ depends on the actual argument of $\sigma_{xy}(\bar{\omega})$. The latter equation describes a field elliptically polarized with main axes along x and y (i.e., $\theta_F = 0$). We thus see that although no Faraday rotation occurs when Eq. (B6) is fulfilled, the polarization changes from linear to elliptic, an unavoidable consequence for Lorentz force enforces some radiation to be emitted that is polarized along the y axis.

In order to determine the field after the second passage, and hence demonstrate our point, i.e., that some Faraday rotation must be necessarily produced in multiple passages through graphene (such as in a cavity geometry), we make use of the transfer matrix formalism. Indeed, we approximate the total $T-$matrix by $\hat{T}_\tau^{\mathrm{graph}}\cdot\hat{T}_\tau^{\mathrm{graph}}$ (this approximation is exact when the phase for free propagation in between the graphene sheets, $\omega W/c$, equals $2m\pi$). Employing Eq. (A7), we obtain,

$$\boldsymbol{E}_2 = \frac{E_0 e^{-i\bar{\omega}t}}{[1+2\beta_+(\bar{\omega})][1+2\beta_-(\bar{\omega})]}\times \\ \times\left\{[1+Z_0\sigma_{xx}(\bar{\omega})]\boldsymbol{e}_x - Z_0\sigma_{xy}(\bar{\omega})\boldsymbol{e}_y\right\}. \quad \text{(B8)}$$

This time, the condition for zero Faraday rotation,

$$\mathrm{Arg}\left[\frac{1+Z_0\sigma_{xx}(\bar{\omega})}{Z_0\sigma_{xy}(\bar{\omega})}\right] = \pm(2m+1)\frac{\pi}{2}, \quad \text{(B9)}$$

cannot be fulfilled because Eq. (B6) fixes the photon frequency in this example. Then, a finite (non-zero) Faraday rotation is produced in the second passage.

The case of graphene in a cavity geometry is more involved because intra-cavity interference takes place. Nevertheless, the physics behind the boost of Faraday rotation is analogous: if, for graphene subjected to a transverse magnetic field, it turns out that the first photon passage yields $\theta_F = 0$, then, it must be in the following passages that $\theta_F > 0$ — see for instance, Eq. (107), valid for an optical cavity made of mirrors with very high reflection amplitudes: because $|\sigma_{xy}(\omega)| > 0$, for $B > 0$, then $\theta_F > 0$ for all light frequencies.

3. Row of graphene sheets

Taking a number N of graphene sheets separated by W, such that $\omega W/c = 2m\pi$, leads to the following electric field, right after the last graphene plane,

$$\boldsymbol{E}_N = E_0 e^{-i\omega t}\left[\frac{1}{1+N\beta_-}\boldsymbol{e}_+ + \frac{1}{1+N\beta_+}\boldsymbol{e}_-\right], \quad \text{(B10)}$$

and hence in the limit $N \gg 1$ we obtain,

$$\frac{t_+}{t_-} \simeq \frac{\sigma_+(\omega)}{\sigma_-(\omega)}, \quad \text{(B11)}$$

which coincides with the result obtained for the cavity-graphene system, given by Eq. (107).

Appendix C: Regularization of the EOM optical conductivity

The EOM approach consists in extracting the optical conductivity from the average of the current operator $\boldsymbol{J}(t)$ (obtained through the corresponding Heisenberg equation).

This method avoids the calculation of current correlations, and hence short-circuits the calculation of $\sigma_{ij}(\omega)$. The crucial point of the EOM approach is the regularization of the following expression,

$$\psi_{ij}(\omega) = \frac{\tilde{J}_i(\omega)}{\tilde{E}_j(\omega)}, \quad \text{(C1)}$$

where $\tilde{O}(\omega)$ ($O = \boldsymbol{J}, \boldsymbol{E}$) is defined via

$$O(t) = \tilde{O}(\omega)e^{-i\omega t} + \text{c.c.}. \quad \text{(C2)}$$

Eq. (C2) is valid for a monochromatic electromagnetic field $\mathbf{A} = \boldsymbol{A}_0 e^{i\omega t} + \text{c.c.}$, and for EOM solutions $\tilde{J}_i(\omega)$ in first order in $\boldsymbol{A}_0$. For convenience, we write the external electric field as $\mathbf{E}(t) = \boldsymbol{E}_+(t) + \boldsymbol{E}_-(t)$, with $\boldsymbol{E}_\pm(t) = \pm i\omega \boldsymbol{A}_0 e^{\mp i\omega t}$.

Despite the resemblance of Eq. (C1) to the Ohm's law, $\psi_{ij}(\omega)$ is not the optical conductivity: in the linear response regime, the EOM solution can be put into the form

$$\boldsymbol{J}(t) = \hat{\psi}(\omega)\boldsymbol{E}_+(t) + \text{c.c.}, \quad \text{(C3)}$$

with $\hat{\psi}(\omega)$ as defined in Eq. (C1). On the other hand, the conductivity, $\hat{\sigma}(t)$, is defined via the relation

$$\boldsymbol{J}(t) = \int_{-\infty}^{\infty} d\tau \hat{\sigma}(t-\tau)\mathbf{E}(\tau). \quad \text{(C4)}$$

The Fourier transform of Eq. (C4) is nothing more than the Ohm's law, $\boldsymbol{J}(\omega) = \hat{\sigma}(\omega)\mathbf{E}(\omega)$, with $\hat{\sigma}(\omega) = \int_{-\infty}^{\infty} dt e^{i(\omega+i0^+)t}\sigma(t)$. The function $\hat{\sigma}(\omega)$ is analytic in the upper complex plane and therefore satisfies Kramers-Kronig causality relations.

From Eqs. (C3)-(C4), we immediately conclude that, $\hat{\psi}(\omega) \neq \hat{\sigma}(\omega)$. The bottom line of the EOM approach is that the tensor $\hat{\psi}(\omega)$ can be exactly transformed into $\hat{\sigma}(\omega)$ via a simple regularization procedure, as we show in what follows.

Without loss of generality let $\boldsymbol{A}_0 = A_0\mathbf{e}_\mathbf{x}$, with $A_0 \in \mathbb{R}$, and consider that no current flows in the absence of external perturbations, $\langle \mathcal{J}_j(t)\rangle = 0$. Since we are interested in the regular part of the optical response, we also take $\mathcal{J}_j(t) = J_j^P(t) \equiv J_j(t)$; then, in first order in A_0,

$$\langle J_i(t)\rangle_H = -\frac{i}{\hbar}\int_{-\infty}^{t} d\tau A(\tau)\langle\big[J_x^I(\tau), J_i^I(t)\big]\rangle_\beta, \quad \text{(C5)}$$

with $i = x, y$. Using the Lehman representation, and similar notation as employed above, the latter expression can be written as,

$$\langle J_i(t)\rangle_H = -\frac{i}{\mathcal{Z}\hbar}\sum_{n\neq m}\int_{-\infty}^{t} d\tau A(\tau)\langle m|J_x|n\rangle\langle n|J_i|m\rangle\times \\ \times e^{i\omega_{mn}(\tau-t)}\left(e^{-\beta E_m} - e^{-\beta E_n}\right). \quad \text{(C6)}$$

Since we wish to find the explicit form of $\hat{\psi}(\omega)$, we perform the integration over the variable τ. We obtain,

$$\langle J_i(t)\rangle_H = \frac{1}{\mathcal{Z}\hbar}\sum_{n\neq m}\frac{1}{\omega+\omega_{nm}+i0^+}\langle m|J_x|n\rangle\langle n|J_i|m\rangle\times \\ \times\left(e^{-\beta E_m} - e^{-\beta E_n}\right)A_0 e^{-i\omega t} + \text{c.c.}. \quad \text{(C7)}$$

where a small imaginary part has been added to ensure convergence. Making use of the definition Eq. (C3), we arrive at the desired result,

$$\psi_{ij}(\omega) = -\frac{1}{\mathcal{Z}\hbar}\frac{1}{i\omega}\sum_{n\neq m}\frac{1}{\omega+\omega_{nm}+i0^+}\times \\ \times\langle m|J_j|n\rangle\langle n|J_i|m\rangle\left(e^{-\beta E_n} - e^{-\beta E_m}\right), \quad \text{(C8)}$$

where $i = x$. We also have $\psi_{xy}(\omega) = -\psi_{yx}(\omega)$.

On the other hand the frequency dependent conductivity is obtained from the Fourier transform of $\sigma(t)$, leading to the well-known Kubo formula

$$\sigma_{ij}(\omega) = \frac{1}{\mathcal{Z}\hbar}\sum_{n\neq m}\frac{1}{i\omega_{nm}}\frac{1}{\omega+\omega_{nm}+i0^+}\times \\ \times\langle m|J_j|n\rangle\langle n|J_i|m\rangle\left(e^{-\beta E_n} - e^{-\beta E_m}\right). \quad \text{(C9)}$$

Comparison of Eq. (C8) with Eq. (C9) yields the general regularization procedure,

$$\sum_{n\neq m}\frac{e^{-\beta E_n} - e^{-\beta E_m}}{\omega}[...] \to \sum_{n\neq m} -\frac{e^{-\beta E_n} - e^{-\beta E_m}}{\omega_{nm}}[...]. \quad \text{(C10)}$$

In a single-electron representation, the Gibbs factors $\mathcal{Z}^{-1}e^{-\beta E_n}$ are substituted for Fermi occupation numbers

$n_F(E_n)$. This procedure was used in Sec. II D to regularize the EOM solutions of graphene in the presence of a magnetic field.

In Sec. II C, no regularization was employed to derive the interband universal conductivity of graphene in zero field, $\mathrm{Re}\,\sigma_{xx}(\omega)$, see Eqs. (21)-(22). The reason is that the $\frac{1}{\omega}$ pre-factor [coming from the electric field $\tilde{E}_x(\omega) = i\omega A_0$] is canceled by numerator in Eq. (C1) in this particular example since, in zero field, $\tilde{J}_x(\omega) \sim \omega$. It is straightforward to show that applying the regularization Eq. (C10) to Eq. (21) yields exactly Eq .(22). As for the imaginary part of the conductivity, the regularization Eq. (C10) is compulsory in order to obtain a consistent result—the imaginary part of Eq. (21), as it stands, diverges.

The regularization prescription Eq. (C10) is general and makes the link between the solutions of the EOM $\hat{\psi}(\omega)$ [Eq. (C3)] and the exact regular optical conductivity $\hat{\sigma}(\omega)$ of electronic systems.

[1] M. Faraday, Phil. Trans. Roy. Soc. London **139**, 1 (1846).
[2] P. R. Berman, Am. J. Phys. **78**, 270 (2010).
[3] E. A. Stern, J. C. McGroddy, and W. E. Harte, Phys. Rev. **135**, A1306 (1964).
[4] E. D. Palik and J. K. Furdynat, Rep. Prog. Phys. **33**, 1193 (1970).
[5] K. S. Novoselov, A. K. Geim, S. V. Morozov, D. Jiang, M. I. Katsnelson, I. V. Grigorieva, S. V. Dubonos, and A. A. Firsov, Nature **438**, 197 (2005).
[6] F. Schedin, A. K. Geim, S. V. Morozov, D. Jiang, E. H. Hill, P. Blake, and K. S. Novoselov, Nat. Mat. **6**, 652 (2007).
[7] N. M. R. Peres, J. M. B. Lopes dos Santos, and T. Stauber Phys. Rev. B **76**, 073412 (2007).
[8] N. M. R. Peres, F. Guinea, and A. H. Castro Neto, Phys. Rev. B **73**, 125411 (2006).
[9] T. Ando, Y. Zheng and H. Suzuura, J. Phys. Soc. Jpn **71**, 1318 (2002).
[10] V. P. Gusynin, and S. G. Sharapov, Phys. Rev. B **73**, 245411 (2006).
[11] V. P. Gusynin, S. G. Sharapov, and J. P. Carbotte, Phys. Rev. Lett. **96**, 256802 (2006).
[12] L. A. Falkovsky and S. S. Pershoguba, Phys. Rev. B **76**, 153410 (2007).
[13] L. A. Falkovsky and A. A. Varlamov, Eur. Phys. J. B **56**, 281 (2007).
[14] T. Stauber, N. M. R. Peres, and A. K. Geim, Phys. Rev. B **78**, 085432 (2008).
[15] N. M. R. Peres and T. Stauber, Int. J. Mod. Phys. B **22**, 2529 (2008).
[16] N. M. R. Peres, Rev. Mod. Phys. **82**, 2673 (2010).
[17] R. R. Nair, P. Blake, A. N. Grigorenko, K. S. Novoselov, T. J. Booth, T. Stauber, N. M. R. Peres, and A. K. Geim, Science **320**, 1308 (2008).
[18] A. B. Kuzmenko, E. van Heumen, F. Carbone, and D. van der Marel, Phys. Rev. Lett. **100**, 117401 (2008).
[19] T. Morimoto, Y. Hatsugai, and H. Aoki, Phys. Rev. Lett. **103**, 116803 (2009).
[20] Y. Ikebe and R. Shimano, Appl. Phys. Lett. **92**, 012111 (2008).
[21] W.-K. Tse, and A. H. MacDonald, Phys. Rev. Lett. **105**, 057401 (2010).
[22] W.-K. Tse, and A. H. MacDonald, Phys. Rev. B **82**, 161104(R) (2010).
[23] J. Karch, P. Olbrich, M. Schmalzbauer, C. Zoth, C. Brinsteiner, M. Fehrenbacher, U. Wurstbauer, M. M. Glazov, S. A. Tarasenko, E. L. Ivchenko, D. Weiss, J. Eroms, R. Yakimova, S. Lara-Avila, S. Kubatkin, and S. D. Ganichev, Phys. Rev. Lett. **105**, 227402 (2010).
[24] S. Yuan, H. De Raedt, and M. I. Katsnelson, Phys. Rev. B **82**, 115448 (2010).
[25] N. M. R. Peres, R. M. Ribeiro, A. H. Castro Neto, Phys. Rev. Lett. **105**, 055501 (2010).
[26] K. v. Klitzing, G. Dorda, and M. Pepper, Phys. Rev. Lett. **45**, 494–497 (1980).
[27] Y. Zhang, Y.-W. Tan, H. L. Stormer, and P. Kim, Nature **438**, 201 (2005).
[28] K. S. Novoselov, E. McCann, S. V. Morozov, V. I.Falko, M. I. Katsnelson, U. Zeitler, D. Jiang, F. Schedin, and A. K. Geim, Nat. Phys. **2**, 177 (2006).
[29] A. Kumar, W. Escoffier, J.M. Poumirol, C. Faugeras, D. P. Arovas, M. M. Fogler, F. Guinea, S. Roche, M. Goiran, and B. Raquet, pre-print: arXiv:1104.1020 (2011).
[30] D. J. Thouless, M. Kohmoto, M. P. Nightingale, and M.den Nijs, Phys. Rev. Lett. **49**, 405 (1982).
[31] V. P. Gusynin, S. G. Sharapov, and J. P. Carbotte, Phys. Rev. Lett. **98**, 157402 (2007).
[32] Y. Ikebe, T. Morimoto, R. Masutomi, T. Okamoto, H. Aoki, and R. Shimano, Phys. Rev. Lett. **104**, 256802 (2010).
[33] I. Crassee, J. Levallois, A. L. Walter, M. Ostler, A. Bostwick, E. Rotenberg, T. Seyller, D. van der Marel, and A. B. Kuzmenko, Nat. Phys. **7**, 48 (2011).
[34] A. H. Castro Neto, F. Guinea, N. M. R. Peres, K. S. Novoselov, and A. K. Geim, Rev. Mod. Phys. **81**, 109 (2009).
[35] A. Ferreira, J. Viana-Gomes, J. Nilsson, E. R. Mucciolo, N. M. R. Peres, and A. H. Castro Neto, Phys. Rev. B **83**, 165402 (2011).
[36] J.W. McClure, Phys. Rev. **104**, 666 (1956).
[37] H. Haug, and S. W. Koch, Phys. Rev. A **39**, 1887 (1989).
[38] N. M. R. Peres, to be published.
[39] Note that the oscillator strength $\tilde{E}_j(\omega)$ of an ac monochromatic external field polarized along j is proportional to the radiation frequency ω and thus Eq. (7) diverges in the dc limit $\omega \to 0$. This ill-behavior is not accidental and stems from the fact that the actual conductivity $\hat{\sigma}(t)$ relates the current at a time t to the external electric field according to $\boldsymbol{J}(t) = \int d\tau \hat{\sigma}(t-\tau)\mathbf{E}(\tau)$, whereas the EOM solution for $\boldsymbol{J}(t)$ rather defines the "EOM conductivity", $\hat{\psi}(\omega)$, satisfying $\boldsymbol{J}(t) = \hat{\psi}(\omega)\mathbf{E}_+(t)$+c.c., where $\mathbf{E}_+(t)$ is the component of the electric field proportional to $e^{-i\omega t}$. As shown in Appendix C, the EOM solution can be regularized to yield the actual conductivity $\hat{\psi}(\omega) \to \hat{\sigma}(\omega)$ according to a general prescription.
[40] T. Stauber, N. M. R. Peres, and A. H. Castro Neto, Phys.

Rev. B **78**, 085418 (2008).
[41] V. P. Gusynin, and S. G. Sharapov, Phys. Rev. Lett. **95**, 146801 (2005).
[42] V. P. Gusynin, S. G. Sharapov, and J. P. Carbotte, Int. Jour. of Mod. Phys. B **21**, 4611 (2007).
[43] A. Pound, J.P. Carbotte, and E.J. Nicol, EPL **94**, 57006 (2011).
[44] J. M. Ziman, Electrons and Phonons, (Oxford University Press, Oxford, 2001).
[45] Neil W. Ashcroft and N. David Mermin, Solid State Physics, (Saunders College, Orlando, 1976).
[46] K. W. Chiu, T. K. Lee, and J. J. Quinn, Surface Science **58**, 182 (1976).
[47] R. F. O'Connell, and G. Wallace, Phys. Rev. B **26**, 2231 (1982).
[48] I. V. Fialkovsky and D. V. Vassilevich, J. Phys. A **42**, 442001 (2009).
[49] Jahan M. Dawlaty, Shriram Shivaraman, Mvs Chandrashekhar, Farhan Rana, and Michael G. Spencer, Appl. Phys. Lett. **92**, 042116 (2008).
[50] M. Breusing, S. Kuehn, T. Winzer, E. Malić, F. Milde, N. Severin, J. P. Rabe, C. Ropers, A. Knorr, and T. Elsaesser, Phys. Rev. B **83**, 153410 (2011).
[51] Jason Horng, Chi-Fan Chen, Baisong Geng, Caglar Girit, Yuanbo Zhang, Zhao Hao, Hans A. Bechtel, Michael Martin, Alex Zettl, Michael F. Crommie, Y. Ron Shen, and Feng Wang, Phys. Rev. B **83**, 165113 (2011).
[52] P. Markoš, and C. M. Soukoulis, Wave propagation: From electrons to photonic crystals and left-handed materials. (Princeton University Press, Princeton and Oxford, 2008).
[53] Y. Zheng, G.-X. Ni, S. Bae, C.-X. Cong, O. Kahya, C.-T. Toh, H. R. Kim, D. Im, T. Yu, J. H. Ahn, B. H. Hong, and B. Özyilmaz, EPL **93** , 17002 (2011).